AGU PUBLICATIONS

JGR

Journal of Geophysical Research: Oceans

RESEARCH ARTICLE

10.1002/2017JC012895

Submesoscale Sea Ice-Ocean Interactions in Marginal Ice Zones

Georgy E. Manucharyan[1] and **Andrew F. Thompson**[1]

[1]Division of Geological and Planetary Sciences, California Institute of Technology, Pasadena, CA, USA

Key Points:
- Energetic submesoscale ocean variability forms at marginal ice zones due to mixed-layer instabilities of ice-edge meltwater fronts
- Mechanical sea ice-ocean interactions trap sea ice in cyclonic eddies and filaments—regions with dramatically enhanced ocean heat fluxes
- The strength of submesoscale sea ice-ocean coupling is expected to increase with thinning of Arctic sea ice and marginal ice zone expansion

Correspondence to:
G. Manucharyan,
gmanuch@caltech.edu

Citation:
Manucharyan, G. E, & Thompson, A. F. (2017). Submesoscale sea ice-ocean interactions in marginal ice zones. *Journal of Geophysical Research: Oceans*, *122*, 9455–9475. https://doi.org/10.1002/2017JC012895

Received 17 MAR 2017
Accepted 25 OCT 2017
Accepted article online 2 NOV 2017
Published online 5 DEC 2017

Abstract Signatures of ocean eddies, fronts, and filaments are commonly observed within marginal ice zones (MIZs) from satellite images of sea ice concentration, and in situ observations via ice-tethered profilers or underice gliders. However, localized and intermittent sea ice heating and advection by ocean eddies are currently not accounted for in climate models and may contribute to their biases and errors in sea ice forecasts. Here, we explore mechanical sea ice interactions with underlying submesoscale ocean turbulence. We demonstrate that the release of potential energy stored in meltwater fronts can lead to energetic submesoscale motions along MIZs with spatial scales O(10 km) and Rossby numbers O(1). In low-wind conditions, cyclonic eddies and filaments efficiently trap the sea ice and advect it over warmer surface ocean waters where it can effectively melt. The horizontal eddy diffusivity of sea ice mass and heat across the MIZ can reach $O(200\ m^2\ s^{-1})$. Submesoscale ocean variability also induces large vertical velocities (order 10 m d^{-1}) that can bring relatively warm subsurface waters into the mixed layer. The ocean-sea ice heat fluxes are localized over cyclonic eddies and filaments reaching about 100 W m^{-2}. We speculate that these submesoscale-driven intermittent fluxes of heat and sea ice can contribute to the seasonal evolution of MIZs. With the continuing global warming and sea ice thickness reduction in the Arctic Ocean, submesoscale sea ice-ocean processes are expected to become increasingly prominent.

1. Introduction

Sea ice cover affects ocean-atmosphere heat fluxes through its dramatic influence on albedo as well as on latent and sensible heat fluxes. Consequently, weather and long-term climate predictions rely significantly on the ability to predict the evolution of bulk sea ice characteristics. As a result of continuing global warming with strong Arctic amplification (Serreze & Barry, 2011), Arctic sea ice properties have dramatically shifted toward smaller thicknesses, lower concentrations, and expanded ice-free regions (Kwok & Rothrock, 2009; Kwok & Untersteiner, 2011; Meier et al., 2007; Serreze & Stroeve, 2015; Stroeve et al., 2012). Additionally, the width of summer marginal ice zones (MIZs)—areas near lateral edges of sea ice extent that have the largest ocean-atmosphere-ice feedbacks—has increased by about 40% over the past few decades (Strong & Rigor, 2013).

Long-term sea ice predictions, e.g., by models participating in the fifth phase of the Coupled Model Intercomparison Project (Taylor et al., 2012), are in significant disagreement between each other (Overland & Wang, 2013; Turner et al., 2013). Seasonal to interannual sea ice predictions are also not robust, with the largest errors concentrated in MIZs (Tietsche et al., 2014). The models are unable to make accurate predictions of sea ice extent for more than several months in advance (Day et al., 2014; Stroeve et al., 2014). The lack of skill in sea ice predictions is, in part, related to the intrinsic stochastic nature of sea ice (Agarwal et al., 2012; Moon & Wettlaufer, 2017) and positive feedbacks in the ocean-ice system (Moon & Wettlaufer, 2011, 2014) as well as to uncertainties in cloud radiative forcing (English et al., 2015; Karlsson & Svensson, 2013). Nonetheless, a majority of models tend to overestimate the sea ice extent (Stroeve et al., 2012), which may imply a model bias due to a misrepresentation of certain processes that transport heat toward the sea ice.

Indeed, ice-mass buoy observations demonstrate that in areas of dramatic sea ice loss, the role of ocean heat flux in sea ice melt has been increasing over the past few decades (Carmack et al., 2015; Polyakov et al., 2017). Part of this response is related to a lengthening of the melt period and increased ocean heat storage due to warmer surface temperatures (Stroeve et al., 2014) and increased solar heating (Perovich et al., 2007). The reduced Arctic sea ice concentrations lead to a more mobile response to atmospheric

winds that increases coupling with the upper ocean and enhances sea ice heating by the Pacific Summer Water (Shimada et al., 2006). Gaining a physical understanding of the processes responsible for extracting heat from the upper ocean requires further investigation.

Because MIZs are regions with dramatic lateral gradients in mixed layer salinity and temperature (e.g., Lu et al., 2015), upper ocean eddies are expected to be prominent there, potentially playing a key role by altering mechanical and thermodynamic sea ice forcing. Strong lateral buoyancy gradients of MIZs facilitate the development of not only mesoscale instabilities but also mixed-layer instabilities that can energize submesoscale variability. Here we refer to submesoscale ocean variability as flows associated with relatively high Rossby numbers, $Ro \sim O(1)$ (compared to mesoscale eddies for which $Ro \sim O(0.1)$). Submesoscale ocean variability is a major component of physical and biological ocean dynamics, characterized by an intense and localized vertical velocity field, narrow fronts and filaments, and enhanced internal wave activity (Boccaletti et al., 2007; Brannigan, 2016; D'Asaro, 1988; Fox-Kemper et al., 2008; Klein & Lapeyre, 2009; Lévy et al., 2012; McWilliams, 1985, 2016; Thompson et al., 2008, 2016).

Signatures of ocean eddies at sea ice margins are indeed evident from satellite imagery as a convoluted ice edge structure with length scales comparable to the oceanic deformation radii (Figure 1). An example from the Beaufort Gyre (Figure 1a) of satellite-derived sea ice concentrations (using Modis/Aqua reflectance data) from September 2016 shows a structure consistent with oceanic eddy variability. The characteristic spatial scales of 10–50 km and persistence times of several days point to coupled dynamics with ocean eddies. A similar example is presented from the Labrador Current (Figure 1b) and Fram Strait (Figure 1c), where satellite imagery suggests that sea ice can be localized in small-scale eddies, filaments, fronts, and wave-like patterns. Although in situ observations are limited, oceanic temperature and salinity structures do suggest the existence of enhanced ocean variability in the vicinity of the MIZ. Underice hydrographic properties from Ice-Tethered Profiler #77 (ITP 77) (http://www.whoi.edu/itp; Krishfield et al., 2008; Toole et al., 2011), which was deployed in the Arctic Ocean and drifted into the Beaufort Gyre MIZ in 2014, is presented in Figure 1d. From the middle of May until the middle of September, the sea ice floe (to which the instrument was attached) experienced dramatic melting and entered the Beaufort Gyre MIZ (see the Ice-Ocean data from the ONR MIZ program). Accompanying this melt was an enhancement of ocean variability (compared to the spring season) that was manifested via large vertical isopycnal excursions, signatures of eddies in the halocline layer, and by enhanced buoyancy variance in the mixed layer (Figure 1d). For ITP 77, Gallaher et al. (2016) report that thermal heterogeneities in the upper ocean lead to intermittent ocean-sea ice heat fluxes reaching magnitudes of O(100–200 W m^{-2}) well away from the ice edge and towards the packed sea ice.

Previous studies have indicated the importance of ocean eddies in MIZs for sea ice and tracer transport as well as for physical-biological interactions (Johannessen et al., 1987a, 1987b; Niebauer & Smith, 1989; Smith & Bird, 1991). Niebauer (1982) argued that the ocean evolution in the presence of melt water fronts and ice-edge upwelling is related to commonly observed high oceanic primary production at the ice edge. Using a coupled ocean and free-drift sea ice model, Häkkinen (1986) explored eddy formation due to wind-driven upwelling/downwelling generated due to a dramatic difference between air-ice and air-water momentum input at MIZs. Downwelling jets were found to be more unstable than upwelling jets with wind reversals necessary for separation of eddies from the ice edge. A more recent study by Lu et al. (2015) showed that instabilities solely due to lateral buoyancy gradients across meltwater fronts could lead to a formation of ocean eddies that induce lateral mixing of heat. Horvat et al. (2016) suggested that the thermodynamic growth/melt of sea ice can depend on the sea ice floe size because of the interactions with ocean eddies. A common message among these studies of ice-edge dynamics is that horizontal buoyancy gradients (either upwelling or melt-driven) can energize strong ocean currents and eddies via baroclinic instabilities. Yet, the above studies did not focus on explaining mechanical coupling of localized and energetic submesoscale eddies with the mobile sea ice.

Here, we propose and quantitatively explore the hypothesis that sea ice mechanics and thermodynamics in MIZs, on relatively small length scales, are significantly affected by the presence of submesoscale ocean variability. In particular, we focus on quantifying the mechanisms of coupling between the sea ice and submesoscale ocean variability on relatively short-time scales (days–weeks) as well as on discussing the implications for the sea ice transport across MIZs and the distribution of ocean-ice heat fluxes. Focusing on submesoscale-sea ice interactions, we consider instabilities of an ice-edge jet that can arise due to horizontal mixed layer buoyancy gradients (melt water fronts) or wind-driven upwelling/downwelling.

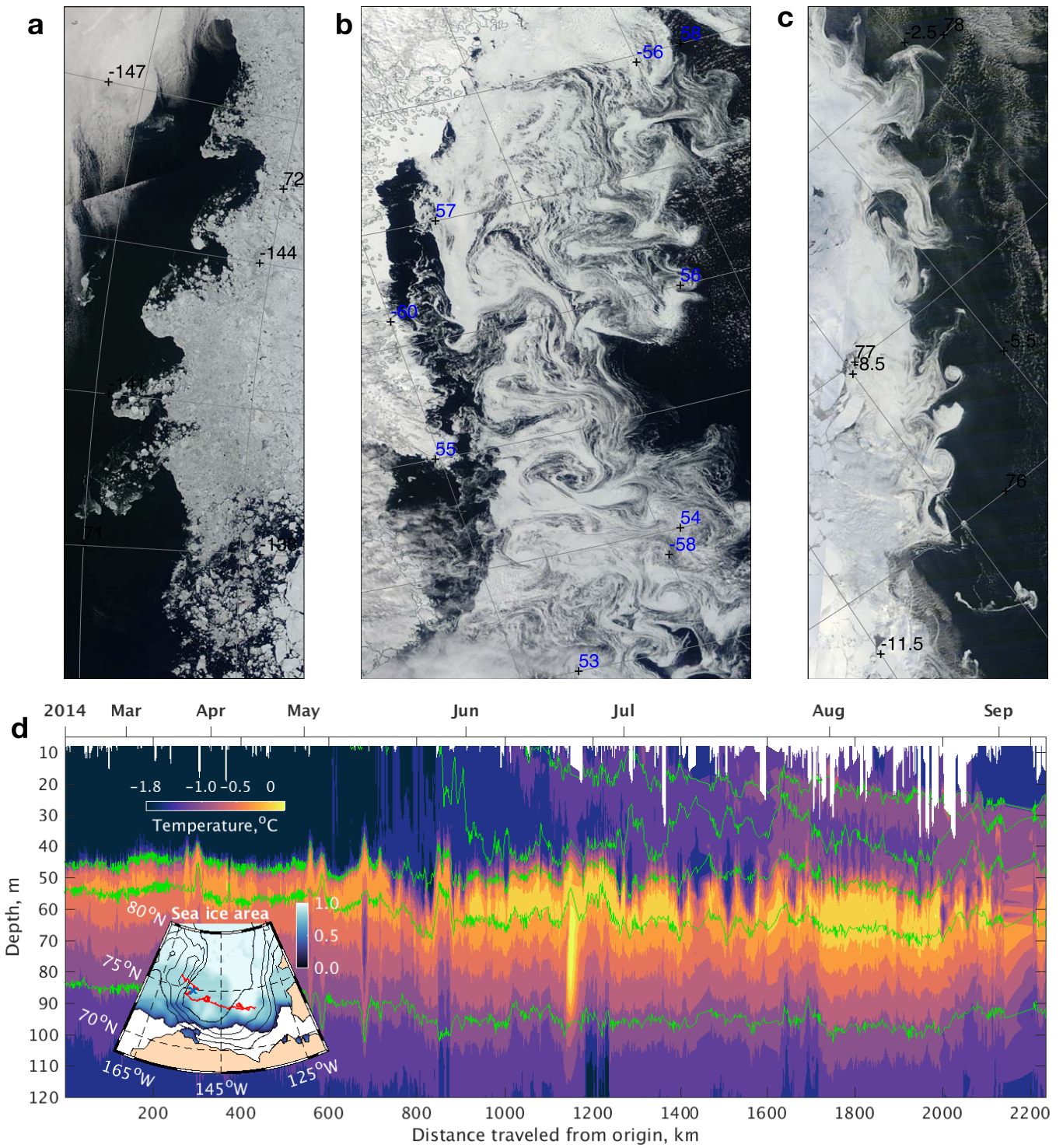

Figure 1. Examples of the MIZs displaying signatures of small scale ocean eddies. (a–c) The Aqua/MODIS corrected reflectance images (worldview.earthdata.nasa.gov) corresponding, respectively, to the Beaufort Gyre MIZ on 9 July 2014, Labrador current of the cost of Labrador (Canada) on 27 April 2016, and Fram Strait on 9 March 2016. Labels denote latitude/longitude and a grid spacing is about 100 km. (d) Ocean hydrography as measured by the ITP 77 (www.whoi.edu/itp), located in the Beaufort Gyre MIZ during year 2014. Colors represent temperature and green contours represent density spaced by 1 kg m^{-3}. Inset shows the ITP track, sea ice concentration map, and 1 km bathymetry contours.

Addressing such a problem presents a challenge because most models treat sea ice as a continuous fluid with rheology that is appropriate for scales large enough to assume statistical equilibrium for mechanical deformation processes (Girard et al., 2011; Hibler, 1979). At length scales of 1–100 km (mesoscales and submesoscales for the Arctic Ocean), individual ice floes can be comparable to the grid size, which questions the validity of sea ice representation as a continuous media. Nonetheless, high-resolution ocean modeling is necessary as eddy-resolving models better represent many of the important physical processes in the ocean including transport of tracers such as heat, salt, carbon, and nutrients. Here, we explore the coupled sea ice-ocean dynamics at characteristic length scales of O(10 km) explicitly assuming that the sea ice floes in MIZs during melting seasons are sufficiently small so as not to affect the continuous assumption. Throughout the paper, we comment on the role of rheology and how an alternative formulation might quantitatively change the results.

In section 2, we present the configuration of an idealized ocean-sea ice model that allows for the formation of ocean eddies through a release of APE stored in the mixed layer. In section 3, we describe the generation of instabilities and the motion of sea ice. In section 4, we explore dynamical ice-eddy interactions and the role of cyclone-anticyclone asymmetry in creating localized sea ice patches. In section 5, we quantify the magnitudes of vertical velocities associated with ocean variability and assess their impact on ocean-sea ice heat fluxes. In section 6, we explore the sea ice transport across fronts and calculate effective sea ice mass diffusivity. The sensitivity of results to model parameters is discussed in section 7. We conclude and discuss implications in section 8.

2. Methodology

2.1. Experimental Philosophy

Dynamics of MIZs are complicated due to a range of interacting processes among which are the small-scale turbulence within the ice-ocean and atmosphere-ocean boundary layers resulting in momentum and heat transport, wind-driven Ekman upwelling/downwelling, buoyancy fluxes from atmospheric heating and phase transitions at the ice-ocean interface, melt water fronts, and surface wave dynamics. Gaining insights into the dynamics of all these processes, simultaneously occurring on a wide range of scales, is challenging. Here, we focus on the mechanisms of sea ice-ocean interactions at submesoscales–dynamics that we expect to be prevalent in MIZs year-round, regardless of particular details of the forcing that generated submesoscale ocean variability in the first place. Therefore, we constrain our experimental design to the simplest case of sea ice-ocean evolution driven by mixed layer instabilities of ice-edge melt water fronts.

Several processes can lead to the formation of sharp melt-water fronts commonly observed near ice edges. These include wind-driven Ekman pumping at the ice-edge boundary, narrow jet formation via mixed layer instabilities of large-scale lateral salinity gradients, and interactions between wind-driven gravity waves with the ice edge. This study, however, is focused on understanding the underlying mechanisms of sea ice interactions with submesoscale turbulence and hence does not aim to represent processes that lead to frontal formation. The idealized simulations to be considered here initialize the MIZ as a localized sharp front that over short-time scales forms eddies and diffuses laterally over a much larger distance than its initial width. By short-time scales, we imply daily or weekly, for which thermodynamic forcing can be neglected because of the dominant role of eddy advection in a background MIZ state with strong lateral gradients.

In the following suite of idealized experiments, we make two substantial simplifications: we do not include the impact of atmospheric winds and thermodynamic sea ice growth/melt. As a result, the dynamics are purely driven by mixed layer gradients of buoyancy, which are known to become unstable and energize submesoscale ocean variability. The buoyancy gradients across the MIZ are driven by the sea ice melt which occurs on large scales because the melt from individual ice floes is spread over a much larger area (compared to floe area) due to the sea ice drift. However, since we are exploring short-time scale MIZ dynamics with the sea ice thermodynamics disabled, the sea ice can only be advected by ocean currents conserving its total volume. In addition, the wind-driven Ekman upwelling/downwelling can displace isopycnals throughout the water column and energize mesoscale eddies of first baroclinic mode—a process that we also exclude in our simulations. Understanding MIZ evolution on longer-time scales (e.g., seasonal) requires a more realistic surface forcing including winds and sea ice thermodynamics.

2.2. Model Configuration

We use a high-resolution ice-ocean model (MITgcm) in its Boussinesq hydrostatic configuration. (Losch et al., 2010; Marshall et al., 1997). The horizontal and vertical resolutions are 0.5 km and 2 m, respectively, chosen to resolve oceanic instabilities arising from horizontal gradients in mixed layer salinity across the MIZ. The vertical resolution increases with depth, up to 50 m at the bottom of the 400 m-deep domain. The model domain is a periodic channel aligned along the MIZ with free-slip boundary conditions in the cross-front direction as well as at the bottom. Since at near-freezing temperatures the thermal expansion coefficient is much smaller than the haline contraction coefficient ($\beta_S = 10^{-3}$), we consider the ocean density to be controlled by its salinity (linear equation of state) with the temperature acting as a passive tracer. This approximation is also justified because of large salinity gradients across MIZs.

The MITgcm equations of motion of sea ice (Losch et al., 2010) are based on its representation as a continuous media:

$$m\frac{\partial \mathbf{u}_i}{\partial t} = -mf\mathbf{k}\times\mathbf{u}_i + \boldsymbol{\tau} - m\nabla\phi(0) + \nabla\cdot\boldsymbol{\sigma}, \tag{1}$$

$$\frac{\partial m}{\partial t} = -\nabla\cdot(\mathbf{u}_i m), \tag{2}$$

$$\frac{\partial c}{\partial t} = -\nabla\cdot(\mathbf{u}_i c), \tag{3}$$

where the index i stands for the ice variables, $m = c\ h$ is the volume of ice per unit area (c is sea ice concentration and h is the mean thickness), $\mathbf{u}$ is the horizontal sea ice velocity, f is the Coriolis parameter, $\boldsymbol{\tau}$ is the ice-ocean stress, $\phi(0) = g\eta + mg/\rho_0$ is the sea surface height potential in response to ocean dynamics and ice loading, and $\boldsymbol{\sigma}$ is the stress tensor representing sea ice rheology (Hibler, 1979). Note that the nonlinear sea ice momentum advection represents a minor contribution in equation (1) and is neglected in the MITgcm sea ice package (Losch et al., 2010).

The driving mechanism for the sea ice motions in our simulations is the ice-ocean stress associated with differences in the speeds between the ice and the upper ocean circulation. The ice-ocean stress in equation (1) is parameterized as

$$\boldsymbol{\tau} = c\rho_0 C_d(\mathbf{u_o} - \mathbf{u_i})|\mathbf{u}_o - \mathbf{u}_i|, \tag{4}$$

where $\mathbf{u_o}$ is the near-surface ocean current, $C_d = 5.6\times10^{-3}$ is a constant drag coefficient that, in general, can vary dramatically depending on sea ice characteristics (Cole et al., 2014). For simplicity, we consider it to be constant, consistent with ECCO2 or SOSE (ECCO2: Estimating the Circulation and Climate of the Ocean, Phase II, Menemenlis et al., 2008; SOSE: Southern Ocean State Estimate, Mazloff et al., 2010) models that underwent a process of data assimilation estimating the best parameters to represent sea ice observations. For a fully developed Ekman spiral, the turning angle for the ocean stress is expected to be relatively small, about 5° for a 5 m deep surface ocean grid box (Taylor & Sarkar, 2008). Additionally, it is reasonable to assume that the Ekman spiral below the moving sea ice is not fully developed for highly transient sea ice motions over strong ocean eddies in MIZ. Thus, the turning angle between the surface ocean velocity and the sea ice velocity is chosen to be zero in our simulations. Note that the stress needs to be scaled with the sea ice concentration because equation (1) represents grid box-averaged sea ice dynamics and hence all forces and accelerations also need to be grid box-averaged. (Not scaling oceanic and atmospheric stresses exerted on the ice with its concentration is a common mistake seen in scientific literature and its consequences are discussed in Connolley et al. (2004). Current version of the MITgcm (c66j) also defaults to an incorrect expression, but does include an option to scale the stress by the concentration (SEAICEscaleSurfStress=.TRUE.) which we have used.).

The SEAICE package in the MITgcm implements Viscous-Plastic (VP) sea ice rheology (Hibler, 1979; Zhang & Hibler, 1997). At high-resolutions (including the 0.5 km used here), formulating the sea ice model via continuous VP equations may not be accurate because some ice floes in MIZ can be of the order of 1 km or larger. A formulation of a continuous high-resolution sea ice model remains an open challenge. Here we consider MIZ dynamics during the melting season where the sea ice floes are observed to be of relatively small sizes, and the ice is loosely packed (Toyota et al., 2006, 2011). In such conditions, the sea ice rheology should not qualitatively affect sea ice advection by ocean eddies. However, throughout the paper, we discuss how

rheology can affect quantitative results. This idealized model configuration is meant to provide insight into the dynamical interactions between submesoscale and mesoscale eddies and a loosely packed sea ice typically observed in the vicinity of melting MIZs.

2.3. MIZ Initialization in a Model

We initialize our idealized model with typical ice-ocean conditions observed at MIZs. In particular, we are interested in simulating ocean dynamics during the melt season characterized by horizontal salinity and mixed layer depth gradients across the MIZ (e.g., Gallaher et al., 2016; Lee et al., 2016). The structure of the initial conditions is shown schematically in Figure 2. We define the depths of the fresher shallower mixed layer as H_m and a denser deeper mixed layer as H_d, the salinity difference across the mixed layer as ΔS, and vertical and lateral temperature differences between the layers as ΔT. Temperature and salinity profiles below the mixed layer are taken as the average of the ITP 77 observations.

The sea ice in MIZs can be either located over the fresher side of the front (Figures 2a and 2b) as in the Labrador Current and Fram Strait or over the saltier and deeper side (Figures 2c and 2d) as in the Beaufort Gyre (Lee et al., 2016). We performed simulations of both of these MIZ configurations and found them to be qualitatively similar. For consistency with the ITP 77 hydrography, we choose our control simulation to correspond to the Beaufort Gyre conditions. Sea ice concentration and thickness transition from $c_0 = 50\%$ and $h_0 = 2$ m at the "northern" side of the computational domain toward zero in the open ocean at the "southern" side:

$$(c, h) = (c_0, h_0)\left[\frac{1}{2} + \frac{1}{2}\tanh\left(\frac{y}{L_f}\right)\right]. \tag{5}$$

Note that the concentration c and the volume hc are both advected by the same sea ice velocity (equations (1)–(3)), and since their initial and boundary conditions have the same functional form, the sea ice thickness h (the ratio of the two fields) remains constant throughout the simulations.

As the sea ice transitions to higher concentrations, its internal stresses start to dominate the dynamics, and mechanical coupling with submesoscale ocean eddies dramatically diminishes. Satellite observations of the Arctic MIZs suggest that the sea ice concentration transitions between 15% and 80% over a distance of

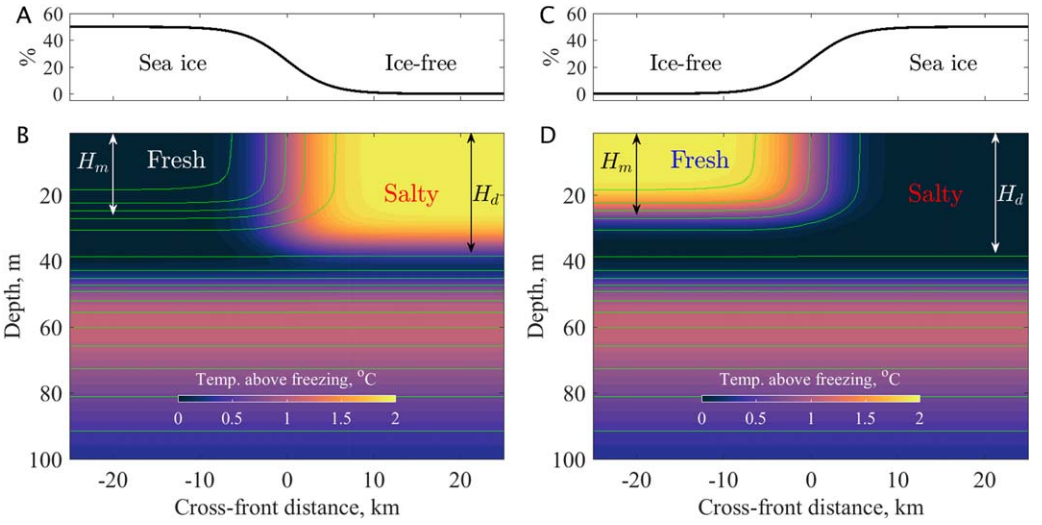

Figure 2. Initial conditions for the coupled sea ice-ocean simulations of a MIZ. (a) Sea ice concentration, c, plotted as a function of cross-frontal distance representing a gradual transition from the ice-free ocean towards a partially ice-covered ocean. (b) Initial ocean stratification initializing a melt-water front with freshwater mixed layer depth, H_m, and saltier deeper mixed layer of depth H_d. Green curves are isohalines with 0.125 intervals; the bulk horizontal salinity difference is 1.2 and the stratification below the mixed layer matches averaged ITP 77 hydrography. This idealized configuration aims to represent MIZs of e.g., Fram Strait or Labrador Current. (c and d) A frontal configuration with the sea ice located over the saltier ocean mixed layer corresponding to conditions representative of the Beaufort Gyre MIZ in 2014 (Lee et al., 2016).

about 100–150 km (Strong & Rigor, 2013). However, here we only consider the sea ice below 50% concentration initially, because we restrict our modeling domain to representing dynamics in a narrow vicinity of MIZs.

The width L_f of the sea ice transition corresponds to the initial width of the ocean front. We choose this width to be of the order of the bulk mixed layer deformation radius $2L_f = 10$ km, emphasizing that the effective frontal width will grow with the development of ocean instabilities.

The ONR-funded MIZ program collected in situ ocean observation demonstrating that lateral buoyancy gradients are ubiquitous features of MIZs (Lee et al., 2016). They report a characteristic bulk salinity difference of about 1–2, and a temperature difference of about 5°C across the 50–100 km MIZ; this corresponds to a characteristic range of large-scale lateral buoyancy gradient of $(1-4)\times10^{-7}$ s^{-2}. The ITP 77 that sampled MIZ of the Beaufort Gyre (discussed in section 1, Figure 1) indeed shows submesoscale activity in the early spring and summer when sea ice melts. The vertical velocities can be estimated from the near-adiabatic isopycnal displacements below the mixed layer; their magnitudes are about 10–30 m d^{-1}.

Since we solve an initial value problem, it is important to justify here the appropriate range of parameters. Assuming that mixed layer freshening below the ice-covered region builds up for a characteristic time scale associated with the development of oceanic mixed-layer instabilities, T_i, a bulk mixed layer salinity change, ΔS, scales as

$$\Delta S \sim S_0 \frac{T_i \dot{h}}{H_m}, \tag{6}$$

where $\dot{h}$ is the sea ice melt rate. Taking numerical values $S_0 \sim 30$, $T_i \sim 10^6$ s, $\dot{h} \sim 5\times10^{-7}$ m s^{-1} (about 30 cm per week during summer season, Gallaher et al., 2016; Perovich et al., 2014), and $H_m \sim 20$ m, we obtain that $\Delta S \sim 0.5$. Since the salinity of the ice-covered ocean does not change significantly (because the sea ice did not melt there yet), ΔS can be considered as a bulk horizontal change in mixed layer salinity across the MIZ. Glider observations in the Beaufort MIZ exhibit salinity differences of $\Delta S \approx 2$ across an $\approx$ 100 km front (Lee et al., 2016) that are qualitatively consistent with ΔS. The large salinity difference from the glider measurements implies that an accumulation of freshwater by continuous sea ice melt may have occurred.

Mixed layer depth and salinity gradients depend on the history of atmospheric winds and sea ice melting rates, which we do not simulate in the idealized model here. Therefore, we explore these effects by initializing a front with a range of parameters. For a control simulation, we use the following frontal parameters: $H_m = 25$ m, $H_d = 35$ m, $\Delta S = 1.2$ (corresponding to about 1 m of sea ice melt), $L_f = 5$ km, and the bulk horizontal temperature difference $\Delta T = 2$ K (Figures 2c and 2d show the control run MIZ configuration). Relevant nondimensional parameters and sensitivity experiments are described in section 7.

3. Eddy Generation in the MIZ

The horizontal buoyancy gradient corresponds to an oceanic APE reservoir that can be efficiently transformed into eddy kinetic energy through different types of ocean instabilities. In the absence of winds, sea ice thickness and concentration are redistributed by the ice-ocean stress. We now proceed to describe the evolution of the emerging oceanic instabilities and their interactions with the mobile sea ice.

Within a few inertial periods, a fluctuating geostrophic current develops within the MIZ which starts shedding eddies on a time scale of several days to a week (Figure 3). The horizontal scale of these submesoscale eddies is 5–10 km, and their radial velocities can reach up to 0.5 m s^{-1} corresponding to a Rossby number $Ro = \xi/f \sim 1$ (the ratio of vertical relative vorticity to the Coriolis frequency, Figure 4). The instability mechanism is consistent with the one described in detail in Manucharyan and Timmermans (2013). The outcropping surface front has high potential vorticity (PV) near the surface and a relatively low potential vorticity below it. These cross-frontal gradients in potential vorticity result in a formation of dipole pairs consisting of surface cyclones and subsurface anticyclones. Subsurface anticyclones, associated with low PV, are subducted into the ice-covered region and are coupled to more intense surface cyclones, associated with high PV originating from the outcrop location. These baroclinic dipoles, also known as hetons (Hogg & Stommel, 1985), result from baroclinic instability and have the ability to self-propagate by advecting each other's PV

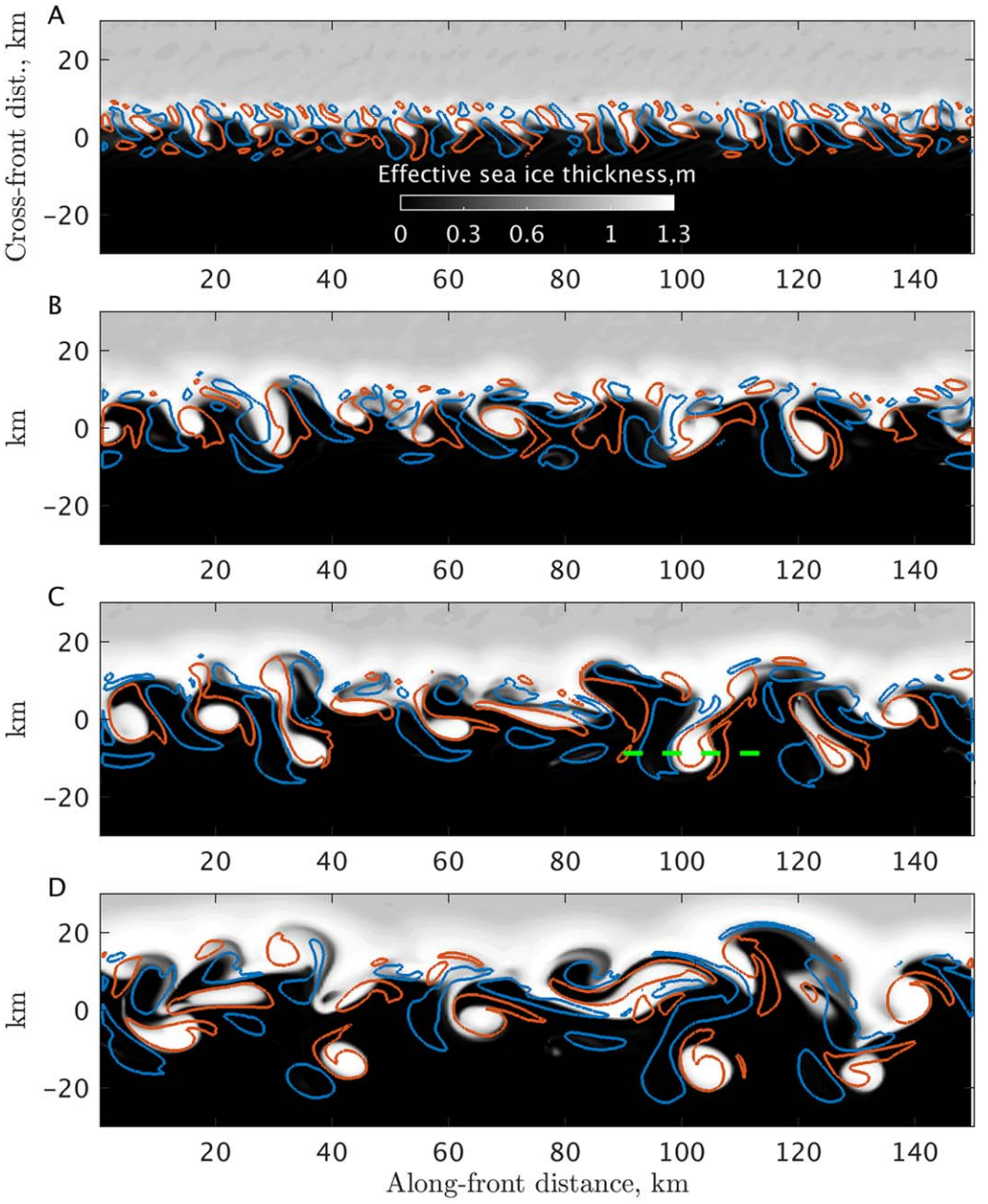

Figure 3. The evolution of MIZ instabilities as simulated by the model for the control run described in section 2.3 and shown in Figure 2. Surface distribution of the effective sea thickness (i.e., thickness times concentration) is plotted in gray scale; black area denotes the ice-free ocean. Contours show mixed layer ocean vorticity of magnitude 0.2 f; red for cyclonic and blue for anticyclonic correspondingly. Figures 3a–3d correspond to model snapshots taken at days 4, 7, 9, and 11. Green-dashed line in plot (c) denotes the location of a transect that is plotted in Figure 4.

anomalies. Manucharyan and Timmermans (2013) discuss how the kinematic trajectories of these dipoles are curved due to an asymmetry in the strength of PV anomalies (surface cyclones are typically much stronger than the anticyclones). The relatively small radius of their semicircular trajectories is a major limiting factor for the cross-frontal dispersion of PV and other tracers, including the sea ice itself.

After about 10 days, the submesoscale eddies are fully energized, and the MIZ evolves into a fully nonlinear phase, where eddy interactions result in a cascade to larger scales with eddy size increasing from several to tens of kilometers (Figure 3). After the spin up, the width of the baroclinic zone becomes more consistent with the in situ observations in the Beaufort Gyre that typically show lateral gradients extending over

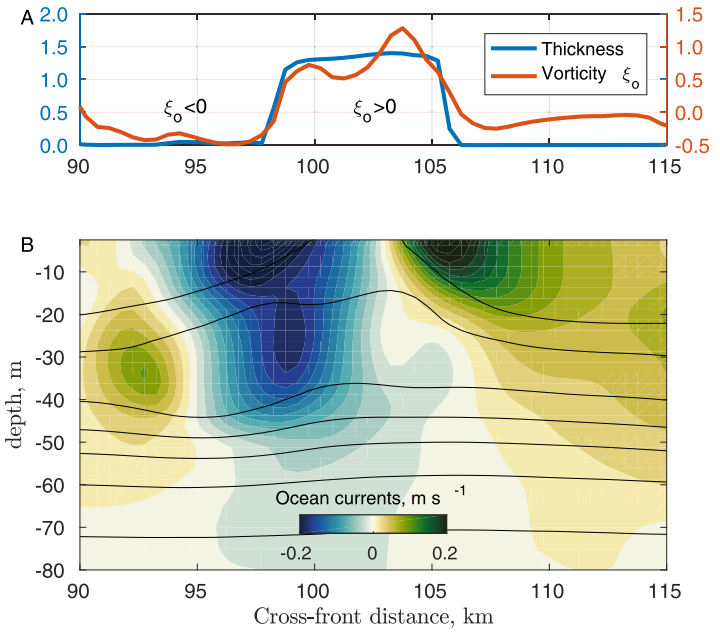

Figure 4. Vertical structure of an ice-covered cyclone taken on model day 11 along the transect shown in Figure 3c with the dashed green line. (a) Effective sea ice thickness (volume per unit area) shown with blue curve (left *y* axis) and the ocean relative vorticity normalized by *f* (red curve, right *y* axis). Note that the sea ice is concentrated over the cyclone. (b) Eddy velocity (perturbation from along-front mean current) along the transect shown with colors (units m s^{-1}, positive is directed out of the page). Isohalines are plotted with black contour lines at 0.125 intervals.

distances of 50–100 km, as well as with satellite-based Arctic MIZ width estimates of about 50–150 km (Strong & Rigor, 2013).

Regions of thin sea ice have relatively small inertia, such that the surface stress induced by the underlying circulation is sufficient to generate sea ice motion. As a result, patterns in the effective sea ice thickness reflect the eddying ocean currents. However, the sea ice does not behave as a passive surface tracer. Instead, the sea ice equations of motions allow for deviations between the ice and surface ocean velocities (1). As discussed below, this behavior partially explains why the sea ice concentrates predominantly in cyclones and persists for as long as the underlying ocean eddy. This sea ice trapping in ocean eddies is an essential process that allows the sea ice to be transferred across the MIZ and leads to conditions favorable for its melting.

4. Dynamics of Ice-Covered Eddies and Filaments

4.1. Constraints on the Relative Sea Ice Motion

All terms in the sea ice momentum equation (1) are directly proportional to the ice volume m except for the stress τ, which is only proportional to its concentration c. In the absence of atmospheric wind stress, this implies that for a thin and loosely packed ice (i.e., with small m), typical for the MIZ, the velocity fields of the ice, and the surface ocean must nearly match to achieve a relatively low surface stress τ. Significant deviations between the ice and surface ocean velocities result in high ocean stress. For sufficiently thin ice, the inertial term ($m\partial u_i/\partial t$) will accelerate the sea ice to reduce τ until other forces, mainly the Coriolis and the rheology, are of comparable magnitude. After the short-term inertial adjustment, i.e., when the sea ice is in a semi-balanced state with the ocean stress, constraints on the discrepancy between the ocean and sea ice motions can be inferred from the following scaling argument. The surface ocean currents are assumed to be in near geostrophic balance $-f\mathbf{k}\times u_o \sim \nabla\phi_0$ and ϕ_0 is the pressure divided by a reference density ρ_0. The Coriolis force is related to the relative sea ice speed and must be balanced by the surface stress

$$-f(u_i-u_o) \sim m^{-1}\tau \sim h^{-1}C_d(u_o-u_i)^2. \tag{7}$$

Using this balance provides a scaling estimate for the relative sea ice velocity, $\Delta u = u_i - u_o$, as

$$\frac{\Delta u}{u_0} \sim \frac{h}{R_d\, Ro\, C_d}, \tag{8}$$

where the Rossby number $Ro \sim u_o R_d^{-1} f^{-1}$. Taking typical values for $f = 10^{-4}$ s^{-1}, $h = 2$ m, $R_d \sim 5$ km, $Ro = 0.5$, and $C_d = 5.6\times10^{-3}$, the nondimensional number in equation (8) is relatively small $\Delta u/u_0 \sim 0.14$ and decreases for higher drag coefficients or thinner sea ice. The numerical simulations confirm that the relative sea ice velocity and vorticity are indeed small compared to typical velocity and vorticity scales associated with the submesoscale eddies (see Figures 5a and 5b). Because this parameter remains relatively low, the ice responds strongly to the underlying small-scale ocean currents with $Ro \sim O(1)$.

The sea ice momentum balance becomes more complicated when substantial atmospheric wind stress can effectively decouple the ocean eddies from the overlying sea ice. As a result, the scaling developed for ice-ocean coupling over submesoscale eddies (8) does not hold. Nonetheless, the variability in atmospheric winds occurs on much larger spatial scales compared to that of ocean eddies, and hence the winds do not provide a strong vorticity source for the sea ice leading to its large-scale relatively irrotational motion. Since the sea ice momentum builds up on inertial time scales, the vorticity impact from individual ocean eddies is weakened for drifting sea ice. Instead, sea ice vorticity would reflect an average ocean forcing (with contributions from both cyclonic and anticyclonic eddies) over a length scale that sea ice moves

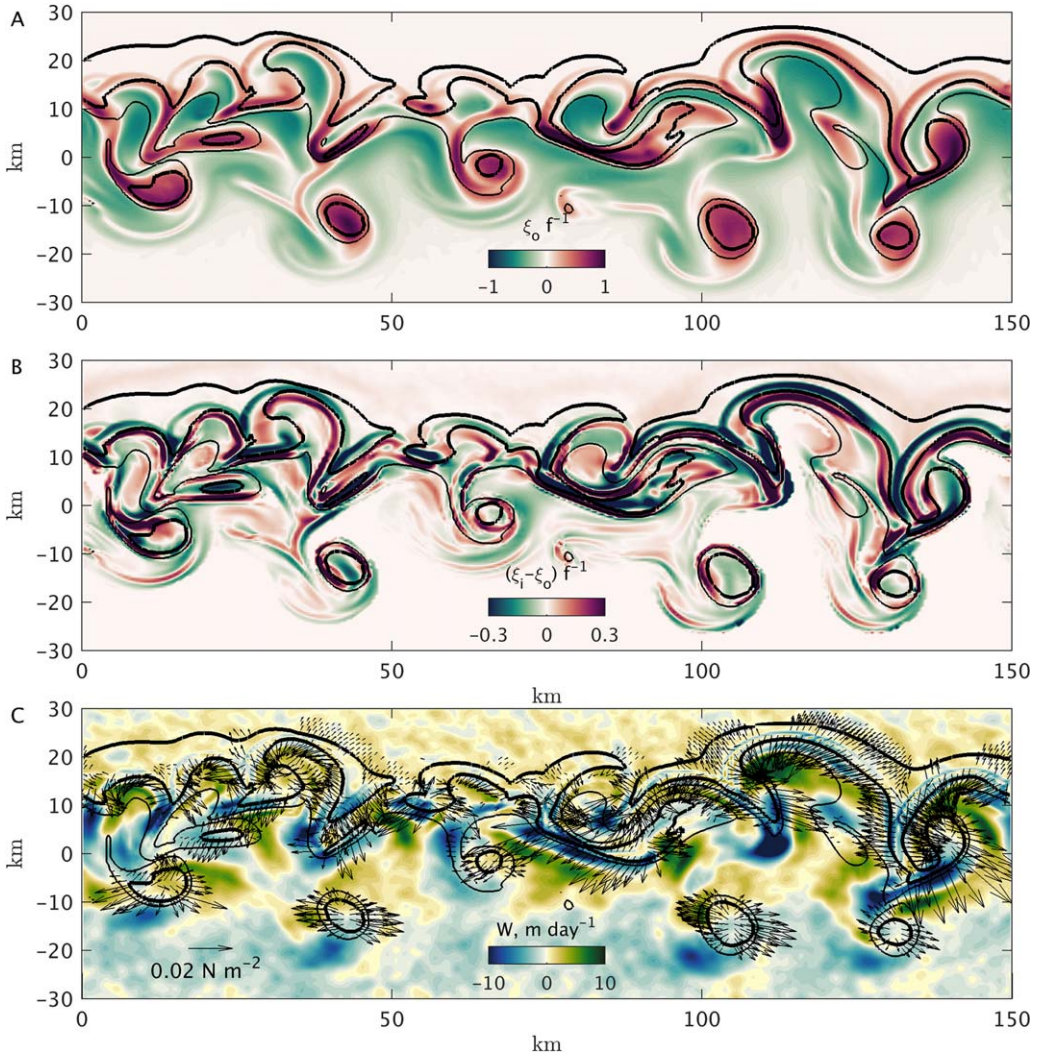

Figure 5. Sea ice-ocean state at model day 11 showing the preferential accumulation of sea ice in cyclonic filaments and eddies and the associated internal sea ice stresses that counteract the accumulation. (a) Surface ocean vorticity normalized by the Coriolis parameter f (colors) and effective sea ice thickness (contour lines of 0.25 and 1.25 m). Strong cyclonic eddies with Rossby numbers $\sim O(1)$ trap the sea ice, whereas anticyclonic eddies repel the sea ice. (b) Difference between the sea ice vorticity and the ocean vorticity normalized by f (colors). Note, a dramatic reduction in color bar scale compared to plot (a) implies a small (but important) difference between sea ice and ocean currents, consistent with a nondimensional coupling parameter (8). (c) Vertical velocity field (colors) at a depth of 25 m where it is usually maximized. The divergence of the internal sea ice stress tensor $\nabla\sigma$ is shown in vectors (largest arrow size corresponds to a magnitude of 0.045 N m^{-2}).

within an inertial time scale. Thus, the vorticity input from a particular ocean eddy can be efficiently transferred if the sea ice translates at a speed slower than $L_{eddy}T^{-1} \approx 0.2$ m s^{-1}, where $L_{eddy} \approx 10$ km is the eddy length scale and $T \approx 4\times10^4$ s is the inertial time scale (half a day for the poles). Incidentally, characteristic sea ice drift speed in the Arctic Ocean is also of the same order of magnitude (Park & Stewart, 2016), implying that the vorticity input from ocean eddies might be significant even in the presence of average winds. We note, however, that the discussed vorticity input applies only to a fraction of the Arctic sea ice for which rheology effects are relatively small, e.g., for low concentration and highly fractured sea ice commonly observed in MIZs.

4.2. Cyclone-Anticyclone Asymmetry in Sea Ice Cover

In addition to an asymmetry between ocean cyclones and anticyclones arising in ice-free conditions (Manucharyan & Timmermans, 2013), the numerical simulations show that sea ice accumulates preferentially in

cyclonic eddies (Figures 3 and 4a). Because sea ice is a buoyant tracer trapped at the surface, its distribution is directly affected by surface ocean divergence. The dominant regions of convergence are the cyclonic submesoscale ocean filaments which trap the sea ice (Figures 5a and 7b). The scale of vertical flow in these filaments is consistent with the confluence-driven frontogenesis theory (Hoskins et al., 1978; Lapeyre & Klein, 2006) reaching magnitudes of about 10 m d^{-1} (Figure 5c). However, in cyclonic eddies, the confluence-driven downwelling is not colocated with the sea ice (Figure 5c) and the frictional sea ice stresses play a key role in its accumulation.

The behavior is related to the dynamical response of the sea ice that amplifies the existing asymmetry in eddies. Near centers of energetic cyclones, the sea ice vorticity is slightly weaker than the ocean eddy vorticity producing an Ekman spin-down; near its edges, the sea ice stress acts to accelerate the ocean (Figure 5b). Surface ocean convergence ($\nabla_h\ u_o = -\partial w/\partial z$) consists of two types of ageostrophic circulations: confluence-driven frontogenesis (Hoskins et al., 1978) and frictional Ekman boundary layers (Ekman, 1905). We can estimate the relative contribution of Ekman transport to surface convergence as $-\partial w_{Ek}/\partial z \approx curl(\tau\rho^{-1}f^{-1})/\Delta z_1$, where $\Delta z_1 = 2$ m is the depth of the top ocean grid box (note, the model does not resolve the turbulent Ekman spiral and most of the Ekman transport occurs in the top grid box). In cyclonic eddies, the ice-stress-driven Ekman pumping is the dominant process that generates surface ocean convergence, while the remaining confluence-driven convergence is maximized outside the sea ice (Figure 6). On the other hand, in filaments, frontogenesis-induced convergence dominates Ekman pumping (not shown).

The sea ice resists this accumulation tendency in cyclonic eddies and filaments via internal stresses associated with the interactions between individual ice floes (shown schematically in Figure 7). As a result, a quasi-steady elevated sea ice mass distribution can be reached. The opposite occurs over anticyclones resulting in divergent Ekman transport, but with a key difference. In this case, the advection of sea ice is not arrested by internal stresses; the sea ice is free to leave the boundary of the eddy. As a result, anticyclonic eddies and filaments exhibit a reduced (or nearly absent) sea ice concentration. There are further feedbacks. Because the mass of sea ice in anticyclones is reduced, the sea ice and ocean velocities will be more closely matched, as suggested by the scaling in (8), and the surface stress will be reduced. This reduction in the ice-ocean stress provides a negative feedback that stabilizes the sea ice concentration in anticyclones and reduces the Ekman divergence. In contrast, for cyclones that have a relatively high sea ice thickness and concentration, the ocean stresses can be larger, thus supporting a stronger Ekman circulation and a greater downwelling in the center of an eddy.

Although the discrepancy between the ocean and sea ice velocities tends to be small, this nonlinear ice rheology produces a dramatic asymmetry between the sea ice cover over cyclonic and anticyclonic eddies. Quantifying the extent of this asymmetry in nature would ideally require simultaneous observations of sea ice concentration and ocean vorticity, although signatures of cyclone-anticyclone asymmetry can also be seen from satellite images. For example, common features of rotating turbulence are self-propagating

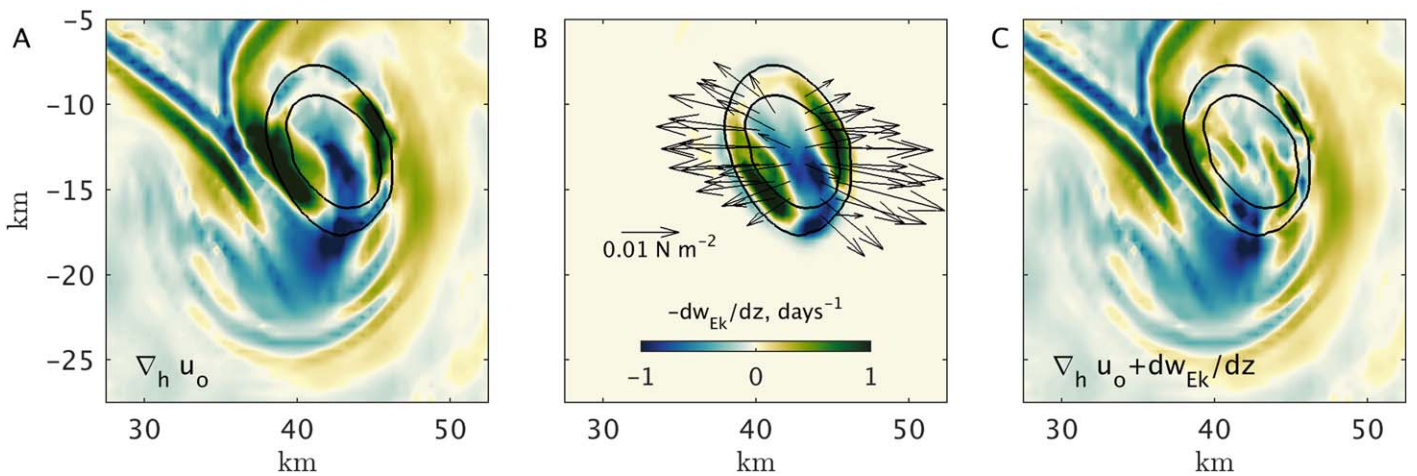

Figure 6. Contribution of the Ekman pumping to the sea ice accumulation in a typical cyclonic eddy demonstrated for the eddy located around (40–20 km) in Figure 5. (a) Horizontal divergence of surface ocean currents ($\nabla_h u_o$). (b) Contribution to the divergence from the Ekman pumping ($-dw_{Ek}/dz$), and (c) the remaining contribution ($\nabla_h u_o + dw_{Ek}/dz$) associated with the confluence-driven vertical velocities and internal gravity waves. All plots share the same color bar shown in plot (b). The sea ice volume is shown in black contours (0.25 and 1.25 m), while arrows in plot (b) represent the divergence of the sea ice stress tensor, same as in Figure 5.

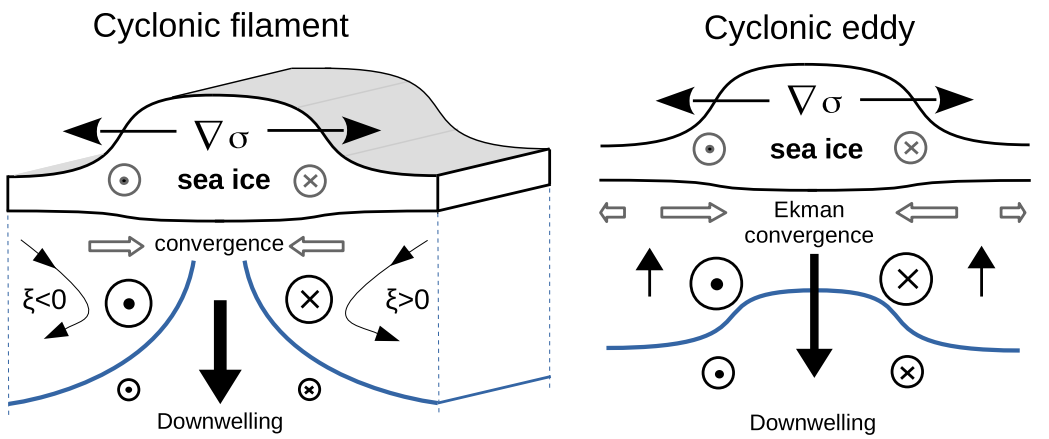

Figure 7. A schematic view of the key mechanisms of sea ice convergence in cyclonic filaments and eddies (Northern hemisphere is assumed, $f > 0$). Cyclonic filaments have strongly convergent surface flows, which accumulate and trap the sea ice. The pressure forces due to the internal sea ice stresses are directed outward to counteract the accumulation. Over cyclonic eddies, the sea ice vorticity is smaller than the vorticity of the underlying eddy near its center, but it is larger near the edges. The resulting surface stresses cause surface Ekman convergence (downwelling near center and weak upwelling at the edges of the eddies). The relative contribution of the ice-stress-driven Ekman pumping compared to the confluence-driven surface convergence is large in near-symmetric coherent eddies, but small in the filaments. The opposite dynamics occur for anticyclonic eddies and filaments that have diverging surface ocean currents and a reduced sea ice volume (not shown in the schematic). Note that the ice rheology is negligible in the case of divergence, and hence cannot counteract the ice loss, resulting in very low sea ice concentrations inside anticyclones.

dipoles (cyclone-anticyclone pairs) which have a wake pointing away from its propagation direction. Several features resembling the ice-covered dipoles can be seen in Labrador current images (Figure 1b), with cyclones having high sea ice concentrations and anticyclones having significantly less (or almost no) sea ice.

Critically, the sea ice rheology and the existence of ice-ocean stress fundamentally changes the behavior of sea ice from that of a passive buoyant tracer. Unlike a passive tracer, sea ice induces an Ekman transport such that its concentration does not purely depend on advection. This property is not qualitatively sensitive to specific rheological parameters of the sea ice as long as these forces remain relatively small compared to ocean-ice stresses. However, the rheology does become important inside cyclonic eddies and filaments that squeeze the sea ice to a finite concentration and thickness. Without the rheology, sea ice would concentrate to very small regions in points of maximum surface convergence.

5. Eddy-Induced Vertical Velocities and Heat Fluxes

In addition to the heat stored in Atlantic water masses below the Arctic halocline, waters just below the near-freezing ice-covered mixed layer are typically a few degrees warmer (see Figure 1d, ITP 77 temperature data). Stable stratification at the base of the mixed layer traps this subsurface heat and limits thermodynamic interactions with the sea ice. However, an energetic submesoscale field is characterized by the intensification of vertical velocities due to both a breakdown of geostrophic balance and various instabilities (Fox-Kemper et al., 2008; Taylor & Ferrari, 2010; Thomas et al., 2008). These intensified vertical velocities can advect subsurface waters into the mixed layer where diabatic mixing can bring this heat into contact with the sea ice. Since the sea ice melt rate is very sensitive to ocean heat fluxes, it is important to understand whether the submesoscale eddies in the MIZ are energetic enough to upwell these deeper waters.

5.1. Vertical Velocities in MIZs

As mixed layer instabilities develop, the vertical velocities in localized filaments can reach values up to 35 m d^{-1} (Figure 8a). Vertical velocities of this magnitude are common for submesoscale eddies, and their formation has been explained in many past studies, e.g., Boccaletti et al. (2007); Thomas et al. (2008). The vertical velocity field is asymmetric, being biased toward intense and compact downwelling in the core of surface cyclones with weaker, but broader upwelling regions surrounding them. Since a near-surface downwelling implies a converging surface ocean flow, the sea ice mass accumulates near these spots of intense

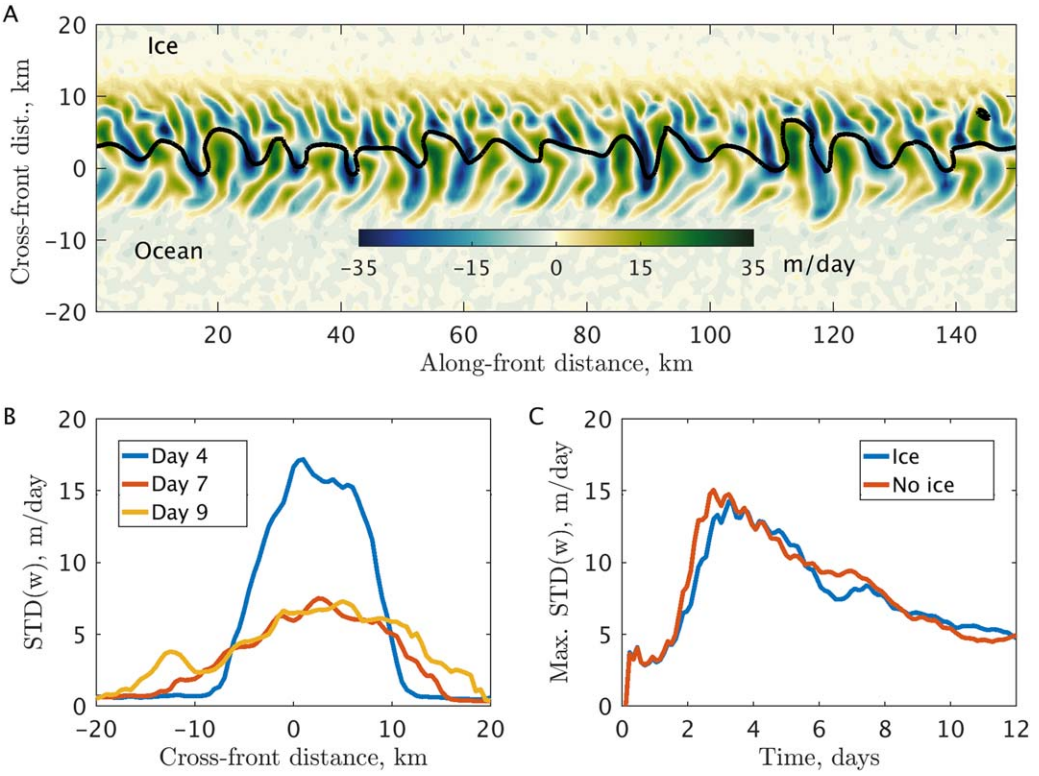

Figure 8. Spatial and temporal variability of vertical velocity for the control simulation (see Figure 3). (a) Vertical velocity at a depth of 12.5 m (in the middle of melt water mixed layer) plotted at model day 4 near the peak of submesoscale activity. Black contour line shows sea ice edge location. (b) Standard deviation of vertical velocity as a function of cross-front coordinate plotted for model days 4, 7, and 9. (c) Time series of the peak standard deviation of vertical velocity showing the development of strong submesoscale activity followed by their inverse cascade toward larger-scale eddies and weaker vertical velocities. Control simulation plotted in blue. Same configuration but without the sea ice is plotted in red showing that ocean instabilities evolve largely independent of the sea ice.

downwelling. This is consistent with our previous discussion of the sea ice being preferentially trapped in cyclonic eddies. The submesoscale instabilities and corresponding vertical velocities become fully developed over a period of about 5 days, and are focused at the core of the MIZ. The STD of the vertical velocity in the MIZ peaks at about 15 m d^{-1} and decreases as the simulation continues (Figure 8c). The most intense vertical velocities occur during the instability development and depend on the initial front characteristics. However, vertical velocities at later stages are sufficient to displace warm water masses vertically into the mixed layer over a time scale of a day. Vertical mixing processes occurring within the mixed layer itself would then heat the near-surface layer and accelerate the sea ice melt. However, depending on the efficiency of the ocean-sea ice heat exchange, only a fraction of the heat brought by eddies into the mixed layer would eventually be absorbed by the sea ice (see discussions in section 5.2).

Due to nonlinear interactions between the MIZ eddies, an inverse energy cascade causes submesoscale eddies to become larger in size and more persistent, with the magnitude of both horizontal and vertical velocities reduced. Thus, at day 10 of the model simulation, the standard deviation of the vertical velocity field decreases to about 6 m d^{-1} and is spread over the entire sea ice transition area (about 30 km around the MIZ, Figure 8b). In nature, the process of eddy formation occurs continuously, reinforced by buoyancy fluxes due to sea ice melting or freezing. Here, the potential energy expends and eddy production ceases because there is no buoyancy forcing that can maintain the front; eddies continue to impact the sea ice distribution and surface heat flux after this time due to eddy memory (Manucharyan et al., 2017).

5.2. Ocean: Sea Ice Heat Flux

The heat flux, F_b, at the ocean-sea ice interface is typically parameterized in climate models as

$$F_b = St^* \rho c_p (T_s - T_f) u^*, \quad (9)$$

where $c_p = 4180$ J kg^{-1} °C^{-1} is the heat capacity of water, $\rho = 1025$ kg m^{-3} is density, St^* is the bulk heat transfer coefficient (referred to as a Stanton number), and u^* is a frictional velocity (see a discussion in Thomas, 2016, chapter 5). In this parameterization, u^* is the least constrained parameter because it depends on the energetics of mixed-layer turbulence that is not represented in our idealized model. Observations of the Arctic sea ice suggest that $St^* \approx 6\times10^{-3}$ and u^* takes a range of values 0.001–0.02 m s^{-1} (McPhee, 2008; McPhee et al., 2003). Since the focus of this study is to emphasize the role of submesoscale motions in redistributing the heat, we assume fixed values of $St^*=6\times10^{-3}$ and $u^*=0.005$ m s^{-1} (appropriate for MIZ conditions, Gallaher et al., 2016; McPhee, 1992) and infer the corresponding ocean-sea ice heat fluxes from equation (9). Since we keep the frictional velocity fixed, the ocean-sea ice heat fluxes can only change if the underlying surface ocean temperatures change. Because we do not model the thermodynamic sea ice melt, the diagnosed heat fluxes should be considered an upper bound since the stratification created by the meltwater can suppress the vertical heating.

The spatial distribution of the instantaneous ocean-ice heat flux within the MIZ highlights its dramatic enhancement over cyclonic eddies and filaments (Figure 9). The strong downwelling at the core of the cyclones converges warm ice-free surface waters laterally underneath the sea ice and results in modeled heat fluxes of up to ~100 W m^{-2}. Zonally-averaged ocean heat fluxes within the MIZ are of the order of 10 W m^{-2}, substantially weaker because of the relatively small fractional area occupied by cyclonic eddies. MIZs with sea ice located over the fresher mixed layer exhibit more cyclonic filaments with enhanced heating of sea ice (compare the two plots in Figure 9). The lack of thermodynamic sea ice melt and of the associated mixed layer restratification allows these large ocean heat fluxes to persist. A 100 W m^{-2} heat flux can melt 2 m of sea ice in about a week, a time scale comparable to the development of submesoscale instabilities. This implies that intermittent submesoscale heating and the advection of sea ice into the open ocean may affect the seasonal MIZ evolution. However, quantifying the cumulative eddy effects at such long-time

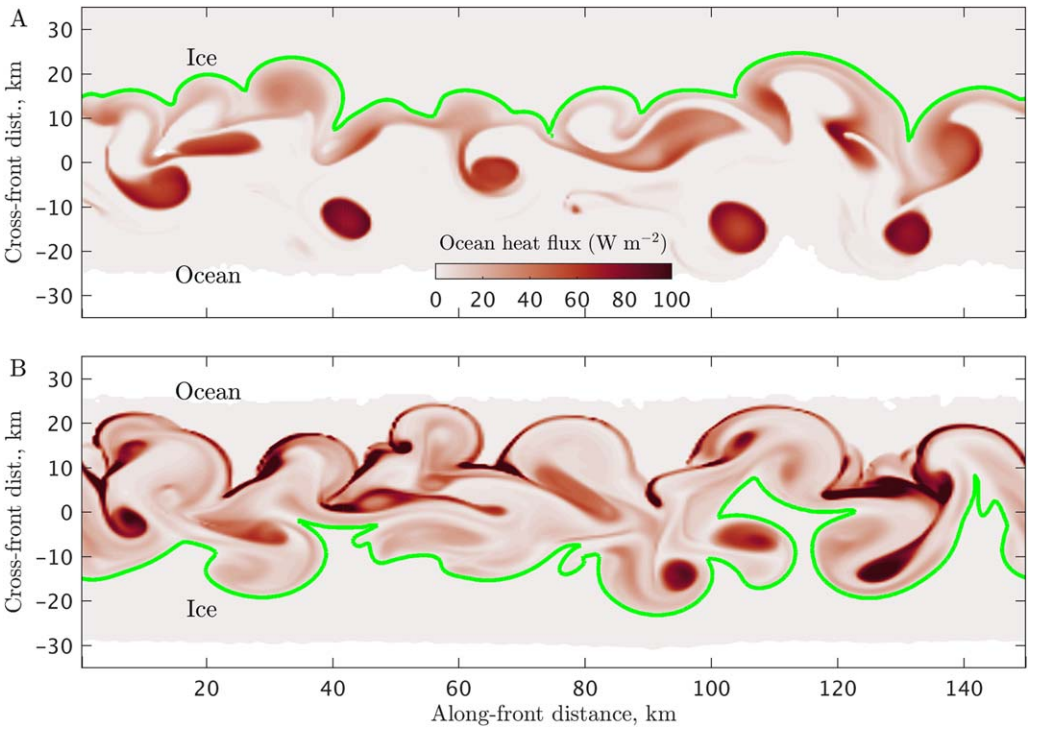

Figure 9. Distribution of the ocean-sea ice heat fluxes (9) at model day 11 for the two MIZ configurations shown in Figure 2. (a) The control simulation with the sea ice located over the saltier mixed layer (Figures 2c and 2d; corresponding snapshot of the sea ice distribution shown in Figure 3d). (b) The MIZ with the sea ice over the fresher mixed layer (Figures 2a and 2b). The green curves correspond to near-freezing temperatures; the white regions at the open ocean side are ice free (effective thickness less than 0.05 m).

scales requires an understanding of their interactions with winds and sea ice thermodynamics that energize the submesoscale variability in the first place.

6. Sea Ice Advection and MIZ Widening by Submesoscale Eddies

In the absence of wind forcing, sea ice velocities within the MIZ closely follow surface ocean currents. Therefore, sea ice that is predominantly trapped in cyclonic eddies can propagate with these eddies. As a result, a relatively narrow MIZ, as was initialized in our numerical simulations, is continuously expanding (Figure 10). As the instabilities develop and eddies grow in size, the sea ice edge (defined as a thickness of 0.05 m) and a surface freezing line ($T_{ocn} \approx T_f$) extend in the cross-front direction (Figure 10 green and black curves). The location of the freezing line is co-located with the extent of sea ice covered eddies (Figure 9) and hence we define the horizontal width of the MIZ, L, as a distance between the freezing line and ice edge. Frontal widening by eddies can be quantified with an effective frontal diffusivity (Taylor, 1922) as

$$K_{front} = \frac{1}{4}\frac{dL^2}{dt} \sim O(200\,\mathrm{m^2 s^{-1}}), \tag{10}$$

considering frontal expansion from 10 to 30 km in about 10 days (Figure 10). While submesoscale vertical velocities peak within the first several days (Figure 8c), frontal widening is most rapid and diffusivities are largest at later stages of instability development when the eddies have grown. The increase in width continues until lateral gradients in mixed layer buoyancy disappear or become too weak to generate eddies. Note that the estimated submesoscale diffusivity is similar than the mesoscale eddy diffusivity of 300 $\pm$200 m^2 s^{-1} in the Beaufort Gyre halocline (Manucharyan et al., 2016). While their characteristics and formation mechanisms are different (mesoscale eddies being larger and deeper but much less energetic than submesoscales), the two types of eddies are similar in that they constrain APE accumulation via lateral freshwater transport (Manucharyan & Spall, 2016).

The advection of sea ice by submesoscale eddies is toward the warmer ice-free waters where it can efficiently melt (Figure 10a). At the same time, there is a transport of warmer waters into the MIZ that further facilitates melting (Figure 10b). Sea ice tongues are evident both from the simulations (Figure 3) and the observed structures (Figure 1). The main sea ice advection mechanism in these simulations is caused by the self-propagation of the oceanic dipole pairs. Since the sea ice is trapped for some time in the ocean eddies, it is propagating perpendicular to the ice concentration gradient. The surface ocean diffusivity will also produce a lateral heat

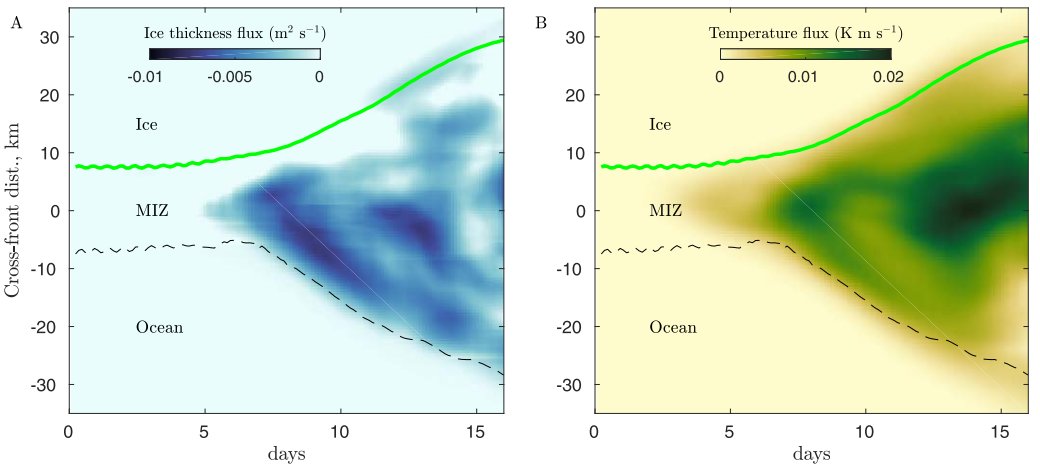

Figure 10. Hovmöller diagrams for zonally-averaged eddy flux of (a) the effective sea ice thickness, F_{ice} (section 6) and (b) horizontal temperature flux in the mixed layer. Negative sea ice thickness and positive temperature fluxes imply a downgradient eddy tracer transport. The green curve denotes the time evolution of the location of zonally-averaged near-freezing surface ocean temperatures; see Figure 9 green curve for an example of its spatial distribution. The dashed black curve denotes the time evolution of the boundary between sea ice and the ice-free ocean; this corresponds to an effective sea ice thickness of 0.05 m. Ocean heat fluxes occur in the expanding MIZ region that is located between the green and the black curves.

transport across the MIZ (Figure 10b). As a result, a portion of the warmer waters from the ice-free ocean penetrates laterally into mixed layer under the sea ice covered regions contributing to melting.

Within the MIZ, the eddy flux of sea ice mass can be defined as $F_{ice}=\overline{v_i' m'}$, where perturbations and averaging are with respect to zonal coordinate and ice mass $m=h\,c$. The flux is downgradient, i.e., thicker sea ice is being transferred toward the open ocean (Figure 10). The process of sea ice dispersion by eddies can also be characterized via an effective horizontal ice thickness diffusivity,

$$K_{ice}=-\frac{<v_i' m'>}{m_y}\sim O(200\,\mathrm{m^2 s^{-1}}), \tag{11}$$

using an ice flux of $F_{ice}=-0.007\ \mathrm{m^2\ s^{-1}}$, the MIZ width of 30 km, and the bulk difference of ice mass of 1 m. The sea ice diffusivity is similar to the frontal diffusivity, which is expected because of the high correlation between the sea ice mass distribution and surface ocean eddies. Note that this strong correlation holds only within the MIZ at relatively low wind conditions and is not expected to occur in thicker, highly-packed sea ice.

The sea ice diffusion acts on a time scale comparable to thermodynamic growth/melt associated with oceanic and atmospheric heating. The climate models that do not resolve submesoscale eddies and only parameterize their effects in the oceanic mixed layer via restratification (Fox-Kemper et al., 2008) are missing the sea ice dispersion that occurs in correlation with ocean heat fluxes within the MIZ (i.e., high heat fluxes are over regions where sea ice mass is concentrated). While submesoscale eddy activity is amplified within the MIZ, it is expected to be significantly damped in heavily packed and relatively immobile sea ice that dampens submesoscale surface flows.

7. Sensitivity to Frontal Parameters

7.1. Relevant Nondimensional Parameters

The ice-ocean coupling is described by the nondimensional parameter $h/(R_d\,Ro\,C_d)$ (8) that can be used to determine regions in the ocean where the dynamics discussed here are relevant. Within a certain vicinity of MIZ, this parameter has to become sufficiently small (due to small sea ice thickness h near the open ocean) to guarantee strong ice-ocean coupling. The lateral extent of this region is determined by the energetics of submesoscale ocean variability, sea ice thickness distribution, and ocean-sea ice drag coefficient, all of which can vary significantly (Lüpkes et al., 2013; Tsamados et al., 2014).

At low concentrations, the sea ice that is strongly strained by the submesoscale eddy field is expected to have a relatively weak contribution from sea ice rheology compared to ocean-ice (or atmosphere-ice) stresses (i.e., $\nabla\boldsymbol{\sigma}\ll\tau$). However, we note that the appropriate range of sea ice concentration and thicknesses that correspond to this weak stress regime would depend on the choice of parameters in the VP model. We will explore this sensitivity in a follow-up study.

The salinity (or density) gradient across the mixed layer provides a reservoir of available potential energy that supports the ocean instabilities and the formation of energetic submesoscale eddies. Manucharyan and Timmermans (2013) considered the evolution of similar outcropping ocean fronts, in an ice-free ocean, and describe the statistical properties of the eddies using two key parameters, the Rossby and Burger numbers. The frontal Rossby Ro_f and the Burger number Bu_f can be defined in terms of the idealized frontal configuration parameters H_m, H_d, and the reduced gravity $g'=g\Delta\rho/\rho_0$:

$$Ro_f=\frac{g' H_m}{f^2 L_f^2},\ \ Bu_f=\frac{g' H_d}{f^2 L_f^2}. \tag{12}$$

The Rossby number measures the relative magnitude of the relative vorticity and the Coriolis parameter f and reflects the importance of geostrophic balance. The Burger number quantifies the width of the front with respect to the Rossby deformation radius $R_d\sim\sqrt{g' H_d}/f\sim O(5km)$. Note that this radius is associated with the mixed layer frontal dynamics and is different from the values commonly calculated using halocline stratification below the mixed layer (e.g., Nurser & Bacon, 2014).

Manucharyan and Timmermans (2013) explored the dependence of ice-free frontal dispersion on the Rossby number (12). In this case, characteristic eddy velocities are directly proportional to the Rossby number (or geostrophic frontal velocity). Thus, the eddy-driven MIZ expansion speed is directly proportional to

the buoyancy gradient $\bar{b}_y$. In turn, the eddy diffusivity is proportional to a square of this gradient since $K \sim dL^2/dt$. As a result, it is clear that the eddy diffusivity should increase with mixed layer depth and horizontal buoyancy gradient as $U_g \sim H_m\, b_y$. Below we emphasize the sensitivity of MIZ fronts to one of the key uncertain parameters, the mixed layer depth H_m on the fresh side of the front (see Figure 2).

7.2. Sensitivity to Mixed Layer Depth

The depth of melt-water layer, H_m, depends on the intensity of mixed layer turbulence and is expected to be smaller than H_d because of the suppressing effect of stratification on mixing (Ivey & Imberger, 1991; Kaneda & Ishida, 2000; Manucharyan & Caulfield, 2015). Thus, we fix $H_d = 35$ m and keep constant the sea ice melt $\Delta h = 1$ m resulting in a varying $\Delta S = S_0 \Delta h H_m^{-1}$. Note, that varying H_m with fixed Δh implies a constant Rossby number, i.e., all fronts would have the same initial magnitude of the surface geostrophic current. However, the available potential energy stored in melt-water fronts (for a fixed Δh) is directly proportional to H_m. Thus, deeper mixed layers (corresponding to smaller Burger numbers) store larger amounts of potential energy and hence can lead to more energetic ocean variability and ocean heat fluxes. Consequently, there is a strong dependence of the MIZ width and vertical velocity statistics on H_m (Figure 11). Shallow fronts ($H_m <\approx 10$ m) take significantly longer to form eddies, and hence their dynamics are likely to be dominated by atmospheric winds and heat fluxes that can change significantly on weekly time scales. On weekly time scales, deeper fronts ($H_m >\approx 20$ m) can transport sea ice mass over a region of about 50 km (Figure 11a). Deeper fronts also generate submesoscale variability on time scales of several days with a variance in vertical velocities order of 10 m d^{-1} (Figure 11b).

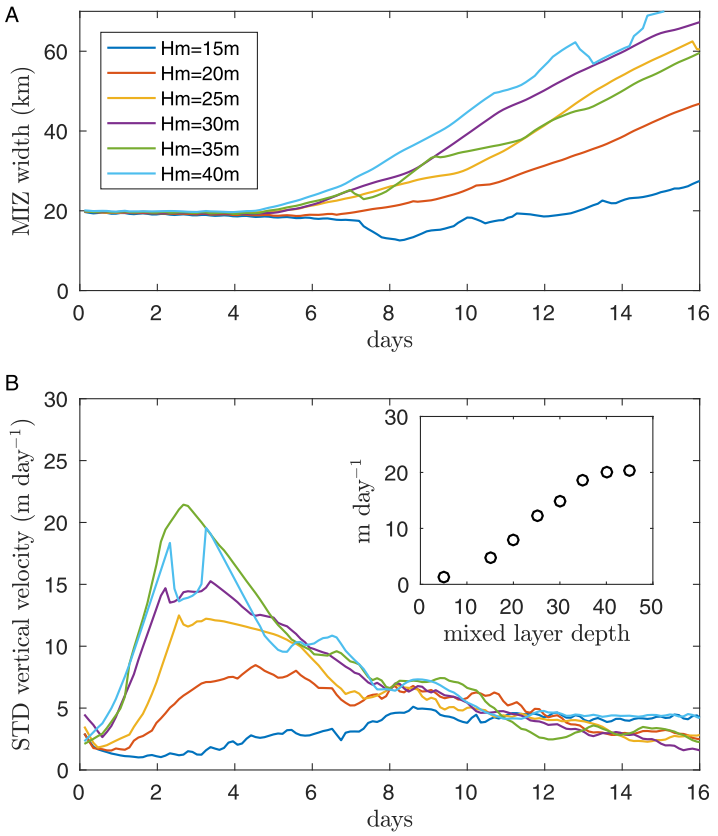

Figure 11. Sensitivity of the meltwater front dynamics to mixed layer depth, H_m, for a fixed amount of large-scale ice melt, as discussed in section 7.2. (a) Time evolution of MIZ width (defined as an area between the ice edge and near freezing surface ocean temperatures as shown in Figure 10). (b) Time evolution of the standard deviation of the frontal vertical velocity in the along-frontal direction. Inset shows the maximum standard deviation of the frontal vertical velocity achieved during the simulation, plotted as a function of the mixed layer depth, H_m. The legend and the colors are consistent between the plots and the inset.

Variations in the Burger number (for a fixed Rossby number) affect the statistical distribution of eddies including the cyclone-anticyclone asymmetry and the mixing length (Manucharyan & Timmermans, 2013). Surface cyclones dominate in fronts with high Burger numbers (12) because a small PV difference in the subsurface layer leads to weak anticyclones. As a result, the dipole pairs propagate via highly curved trajectories and are inefficient in tracer transport, leading to slower frontal widening as seen in Figure 11a. Thus, deeper mixed layers (H_m) lead to more efficient sea ice dispersion and tracer mixing. Consequently, commonly observed melt-water fronts (about 15–30 m deep) store sufficiently large amounts of APE to generate energetic vertical velocities and lateral sea ice dispersion that can expedite the overlying sea ice melt.

8. Conclusions and Discussion

Oceanic conditions in MIZs are characterized by mixed layer buoyancy gradients related to the temporal evolution of sea ice melt and growth. These gradients imply available gravitational potential energy that the ocean can release via a set of mixed-layer instabilities generating energetic submesoscale eddies. The surface ocean currents, reaching velocities up to 0.2 m s^{-1}, can efficiently advect thin and low-concentrated sea ice across a MIZ into the open ocean. The sea ice is predominantly trapped within cyclonic filaments that have strong confluence-driven convergent surface flows and in cyclonic eddies where the frictional Ekman pumping generates convergence. In contrast, anticyclones repel the sea ice. As the baroclinic ocean eddies move across the MIZ front, they also induce a downgradient sea ice transport resulting in a horizontal expansion of the MIZ width. Within a realistic set of frontal parameters, the effective diffusivity associated with the downgradient sea ice transport by eddies is $O(200\ \mathrm{m^2\ s^{-1}})$. The submesoscale ocean eddies are fluxing not only

the sea ice mass but also mixed layer freshwater and heat across the MIZ resulting in substantial warming of the ice-covered ocean.

The modeled submesoscale eddies have vertical velocities of the order of 10 m d^{-1} (Figure 11), consistent with the observational estimates obtained based on isopycnal displacements below the mixed layer in the ITP 77 (Figure 1d). The vertical velocities can bring nutrients upward into the euphotic zone providing favorable conditions for commonly observed ice-edge phytoplankton blooms (Ardyna et al., 2014; Arrigo et al., 2012; Zhang et al., 2015). As a result of the enhanced lateral and horizontal transports, an additional localized ocean heating of the order of 100 W m^{-2} is available to accelerate the sea ice melt or slow down its growth in MIZs. Similar magnitude episodic heating by warm core ocean eddies has been observed in Western Arctic MIZ (Gallaher et al., 2016) more than 150 km from the sea ice edge under 75% ice cover. This suggests that perhaps submesoscale ocean eddies and frontal instabilities occur not only at the ice edge, where they are obvious from sea ice patterns, but eddies may also extend under relatively packed sea ice, which does not reflect the signature of eddies.

Our idealized model does not include atmospheric winds and sea ice thermodynamics and does not simulate the jet formation. Thus, the discussed mechanisms of ice-ocean interactions are most relevant at short-time scales (days to a few weeks) and spatial scales of the order of 10 km. While large-scale and seasonal MIZ dynamics are strongly affected by atmospheric winds (Campbell, 1965; Spreen et al., 2011; Steele & Ermold, 2015; Thorndike & Colony, 1982), we argue that the submesoscale dynamics should be prominent in MIZs and can substantially affect the atmospherically-driven sea ice dynamical and thermodynamical response by modulating the sea ice-ocean heat fluxes. Moreover, the nondimensional parameter describing the extent of ice-ocean coupling (8) indicates that a continuing reduction in the Arctic sea ice thickness due to global warming will lead to enhanced signature of ocean eddies on sea ice. These coupled submesoscale ice-ocean interactions are critical processes that are currently not resolved in climate models and thus require further quantitative theoretical and observational analysis.

Current climate models lack the resolution needed to represent highly localized and intermittent heat and nutrient fluxes and resort to parameterizations to include their effects. Conventionally, mixed layer restratification processes are parameterized in a zonal or ensemble mean sense (Fox-Kemper et al., 2008) by introducing an additional eddy stream function (Andrews & McIntyre, 1976; Gent et al., 1995; Gent & McWilliams, 1990) that acts to slump isopycnals. However, the resulting stream function produces vertical velocities that are weaker than those associated with individual eddies. For nonlinear processes such as sea ice melt, which occurs during positive perturbations in heat fluxes but does not occur during the negative perturbations, this approach misrepresents the average ice-ocean heat flux. Furthermore, the sea ice mass transport and accumulation occurs over cyclonic eddies where there are also large heat fluxes. This correlation implies that sea ice and buoyancy transports in climate models cannot be parameterized as independent processes. Thus, alternative parameterizations are necessary to incorporate the ocean heat fluxes appropriately.

Under further global warming and polar amplification, most IPCC models predict trends toward thinner and less concentrated sea ice, eventually leading to its disappearance. These processes are accompanied by an increase in the areal extent of the MIZ as well as large seasonal variations in the MIZ's position. As a result, the sea ice-ocean coupling at submesoscales should be of increasing significance for a large fraction of the Arctic Ocean. Our study provides evidence that a misrepresentation of the episodic warming by submesoscale eddies in MIZs may limit the accuracy of climate predictions of sea ice characteristics.

Acknowledgments
All information necessary to reproduce the numerical experiments is included in the manuscript; MITgcm name lists and configuration files could be found at http://web.gps.caltech.edu/~andrewt/publications/MIZconfigFiles.tar.gz. G.E.M. and A.F.T. gratefully acknowledge support from the Stanback Postdoctoral Fellowship Fund and the Davidow Discovery Fund at Caltech. The manuscript benefited from discussions at the annual Forum for Arctic Modeling and Observing Synthesis (FAMOS) funded by the NSF OPP awards PLR-1313614 and PLR-1203720. The authors acknowledge the high-performance computing support from Yellowstone provided by the NCAR CIS Laboratory, sponsored by the NSF. This work used the Extreme Science and Engineering Discovery Environment (XSEDE) (Towns et al., 2014), which is supported by NSF grant number ACI-1053575. The authors thank Chris Horvat and the two other anonymous reviewers for their insightful comments that led to improvements of the manuscript.

References

Agarwal, S., Moon, W., & Wettlaufer, J. S. (2012). Trends, noise and re-entrant long-term persistence in Arctic sea ice. *Proceedings of the Royal Society A*, *468*, 2416–2432.

Andrews, D. G., & McIntyre, M. E. (1976). Planetary waves in horizontal and vertical shear: The generalized Eliassen-Palm relation and the mean zonal acceleration. *Journal Atmospheric Sciences*, *33*(11), 2031–2048.

Ardyna, M., Babin, M., Gosselin, M., Devred, E., Rainville, L., & Tremblay, J. E. (2014). Recent Arctic Ocean sea ice loss triggers novel fall phytoplankton blooms. *Geophysical Research Letters*, *41*, 6207–6212. https://doi.org/10.1002/2014GL061047

Arrigo, K. R., Perovich, D. K., Pickart, R. S., Brown, Z. W., Van Dijken, G. L., Lowry, K. E., . . . Bates, N. R. (2012). Massive phytoplankton blooms under Arctic sea ice. *Science*, *336*(6087), 1408–1408.

Brannigan, L. (2016). Intense submesoscale upwelling in anticyclonic eddies. *Geophysical Research Letters*, *43*, 3360–3369. https://doi.org/10.1002/2016GL067926

Boccaletti, G., Ferrari, R., & Fox-Kemper, B. (2007). Mixed layer instabilities and restratification. *Journal of Physical Oceanography*, *37*(9), 2228–2250.
Campbell, W. J. (1965). The wind-driven circulation of ice and water in a polar ocean. *Journal of Geophysical Research*, *70*(14), 3279–3301.
Carmack, E., Polyakov, I., Padman, L., Fer, I., Hunke, E., Hutchings, J., . . . Winsor, P. (2015). Toward quantifying the increasing role of oceanic heat in sea ice loss in the new Arctic. *Bulletin of the American Meteorological Society*, *96*, 2079–2105. https://doi.org/10.1175/BAMS-D-13-00177.1
Cole, S. T., Timmermans, M. L., Toole, J. M., Krishfield, R. A., & Thwaites, F. T. (2014). Ekman veering, internal waves, and turbulence observed under Arctic sea ice. *Journal of Physical Oceanography*, *44*(5), 1306–1328.
Connolley, W. M., Gregory, J. M., Hunke, E., & McLaren, A. J. (2004). On the consistent scaling of terms in the sea-ice dynamics equation. *Journal of Physical Oceanography*, *34*(7), 1776–1780.
D'Asaro, E. A. (1988). Generation of submesoscale vortices: A new mechanism. *Journal of Geophysical Research*, *93*(C6), 6685–6693.
Day, J. J., Tietsche, S., & Hawkins, E. (2014). Pan-Arctic and regional sea ice predictability: Initialization month dependence. *Journal of Climate*, *27*(12), 4371–4390.
Ekman, V. W. (1905). On the influence of the earth's rotation on ocean currents. *Arkiv För Matematik, Astronomi Och Fysik*, *2*, 1–53.
English, J. M., Gettelman, A., & Henderson, G. R. (2015). Arctic radiative fluxes: Present-day biases and future projections in CMIP5 models. *Journal of Climate*, *28*(15), 6019–6038.
Fox-Kemper, B., Ferrari, R., & Hallberg, R. (2008). Parameterization of mixed layer eddies. Part I: Theory and diagnosis. *Journal of Physical Oceanography*, *38*(6), 1145–1165.
Gallaher, S. G., Stanton, T. P., Shaw, W. J., Cole, S. T., Toole, J. M., Wilkinson, J. P., . . . Hwang, B. (2016). Evolution of a Canada Basin ice ocean boundary layer and mixed layer across a developing thermodynamically forced marginal ice zone. *Journal of Geophysical Research: Oceans*, *121*, 6223–6250. https://doi.org/10.1002/2016JC011778
Gent, P. R., & McWilliams, J. C. (1990). Isopycnal mixing in ocean circulation models. *Journal of Physical Oceanography*, *20*(1), 150–155.
Gent, P. R., Willebrand, J., McDougall, T. J., & McWilliams, J. C. (1995). Parameterizing eddy-induced tracer transports in ocean circulation models. *Journal of Physical Oceanography*, *25*(4), 463–474.
Girard, L., Bouillon, S., Weiss, J., Amitrano, D., Fichefet, T., & Legat, V. (2011). A new modeling framework for sea-ice mechanics based on elasto-brittle rheology. *Annals of Glaciology*, *52*(57), 123–132.
Häkkinen, S. (1986). Coupled ice-ocean dynamics in the marginal ice zones: Upwelling/downwelling and eddy generation. *Journal of Geophysical Research*, *91*(C1), 819–832.
Hibler, W. D. III, (1979). A dynamic thermodynamic sea ice model. *Journal of Physical Oceanography*, *9*, 815–846.
Hogg, N. G., & Stommel, H. M. (1985). The heton, an elementary interaction between discrete baroclinic geostrophic vortices, and its implications concerning eddy heat-flow. *Proceedings of the Royal Society of London A*, *397*(1812), 1–20.
Horvat, C., Tziperman, E., & Campin, J.-M. (2016). Interaction of sea ice floe size, ocean eddies, and sea ice melting. *Geophysical Research Letters*, *43*, 8083–8090. https://doi.org/10.1002/2016GL069742
Hoskins, B. J., Draghici, I., & Davies, H. C. (1978). A new look at the ω-equation. *Quarterly Journal of the Royal Meteorological Society*, *104*(439), 31–38.
Ivey, G. N., & Imberger, J. (1991). On the nature of turbulence in a stratified fluid. Part I: The energetics of mixing. *Journal of Physical Oceanography*, *21*(5), 650–658.
Johannessen, O. M., Johannessen, J. A., Svendsen, E., Shuchman, R. A., Campbell, W. J., & Josberger, E. (1987). Ice-edge eddies in the Fram Strait marginal ice zone. *Science*, *236*(4800), 427–429.
Johannessen, J. A., Johannessen, O. M., Svendsen, E., Shuchman, R., Manley, T., Campbell, W. J., . . . Van Leer, J. (1987). Mesoscale eddies in the Fram Strait marginal ice zone during the 1983 and 1984 Marginal Ice Zone Experiments. *Journal of Geophysical Research*, *92*(C7), 6754–6772.
Kaneda, Y., & Ishida, T. (2000). Suppression of vertical diffusion in strongly stratified turbulence. *Journal of Fluid Mechanics*, *402*, 311–327.
Karlsson, J., & Svensson, G. (2013). Consequences of poor representation of Arctic sea-ice albedo and cloud-radiation interactions in the CMIP5 model ensemble. *Geophysical Research Letters*, *40*, 4374–4379. https://doi.org/10.1002/grl.50768
Klein, P., & Lapeyre, G. (2009). The oceanic vertical pump induced by mesoscale and submesoscale turbulence. *Annual Review of Marine Science*, *1*, 351–375.
Krishfield, R., Toole, J., Proshutinsky, A., & Timmermans, M. L. (2008). Automated ice-tethered profilers for seawater observations under pack ice in all seasons. *Journal of Atmospheric and Oceanic Technology*, *25*(11), 2091–2105.
Kwok, R., & Rothrock, D. A. (2009). Decline in Arctic sea ice thickness from submarine and ICESat records. *Geophysical Research Letters*, *36*, L15501. https://doi.org/10.1029/2009GL039035
Kwok, R., & Untersteiner, N. (2011). The thinning of Arctic sea ice. *Physics Today*, *64*(4), 040000, https://doi.org/10.1063/1.3580491
Lapeyre, G., & Klein, P. (2006). Impact of the small-scale elongated filaments on the oceanic vertical pump. *Journal of Marine Research*, *64*(6), 835–851.
Lee, C., Rainville, L., & Perry, M. J. (2016). Upper ocean evolution across the Beaufort Sea marginal ice zone. Paper presented at the Forum for Arctic Modeling and Observational Synthesis (EPSC2016–9227), Meeting #5, Poster C.34, Woods Hole Oceanographic Institution, Woods Hole, MA. Retrieved from http://science.whoi.edu/users/aproshutinsky/2016_FAMOS_Meeting/POSTERS/C34_LeeEtAl_FAMOS2016
Lévy, M., Ferrari, R., Franks, P. J., Martin, A. P., & Rivière, P. (2012). Bringing physics to life at the submesoscale. *Geophysical Research Letters*, *39*, L14602. https://doi.org/10.1029/2012GL052756
Losch, M., Menemenlis, D., Heimbach, P., Campin, J.-M., & Hill, C. (2010). On the formulation of sea-ice models. Part 1: Effects of different solver implementations and parameterizations. *Ocean Modelling*, *33*, 145–158.
Lu, K., Weingartner, T., Danielson, S., Winsor, P., Dobbins, E., Martini, K., & Statscewich, H. (2015). Lateral mixing across ice meltwater fronts of the Chukchi Sea shelf. *Geophysical Research Letters*, *42*, 6754–6761. https://doi.org/10.1002/2015GL064967
Lüpkes, C., Gryanik, V. M., Rösel, A., Birnbaum, G., & Kaleschke, L. (2013). Effect of sea ice morphology during Arctic summer on atmospheric drag coefficients used in climate models. *Geophysical Research Letters*, *40*, 446–451. https://doi.org/10.1002/grl.50081
Manucharyan, G. E., & Caulfield, C. P. (2015). Entrainment and mixed-layer dynamics of a surface-stress-driven stratified fluid. *Journal of Fluid Mechanics*, *765*, 653–667.
Manucharyan, G. E., & Spall, M. A. (2016). Wind-driven freshwater buildup and release in the Beaufort Gyre constrained by mesoscale eddies. *Geophysical Research Letters*, *43*, 273–282. https://doi.org/10.1002/2015GL065957
Manucharyan, G. E., Spall, M. A., & Thompson, A. F. (2016). A theory of the wind-driven Beaufort Gyre variability. *Journal of Physical Oceanography*, *46*(11), 3263–3278.
Manucharyan, G. E., Thompson, A. F., & Spall, M. A. (2017). Eddy-Memory mode of multi-decadal variability in residual-mean ocean circulations with application to the Beaufort Gyre. *Journal of Physical Oceanography*, *47*(4), 855–856. https://doi.org/10.1175/JPO-D-16-0194.1

Manucharyan, G. E., & Timmermans, M.-L. (2013). Generation and separation of mesoscale eddies from surface ocean fronts. *Journal of Physical Oceanography*, *43*(12), 2545–2562.
Marshall, J., Adcroft, A., Hill, C., Perelman, L., & Heisey, C. (1997). A finite-volume, incompressible Navier Stokes model for studies of the ocean on parallel computers. *J. Geophysical Research*, *102*(C3), 5753–5766.
Mazloff, M. R., Heimbach, P., & Wunsch, C. (2010). An eddy-permitting Southern Ocean state estimate. *Journal of Physical Oceanography*, *40*(5), 880–899.
McPhee, M. G. (1992). Turbulent heat flux in the upper ocean under sea ice. *Journal of Geophysical Research*, *97(C4)*, 5365–5379.
McPhee, M. G. (2008). Physics of early summer ice/ocean exchanges in the western Weddell Sea during ISPOL. *Deep Sea Research Part II: Topical Studies in Oceanography*, *55*(8), 1075–1097.
McPhee, M. G., Kikuchi, T., Morison, J. H., & Stanton, T. P. (2003). Ocean-to-ice heat flux at the North Pole environmental observatory. *Geophysical Research Letters*, *30(24)*, 2274. https://doi.org/10.1029/2003GL018580
McWilliams, J. C. (1985). Submesoscale, coherent vortices in the ocean. *Reviews of Geophysics*, *23*(2), 165–182.
McWilliams, J. C. (2016). Submesoscale currents in the ocean. *Proceedings of the Royal Society A 472*(2189), 20160117.
Meier, W. N., Stroeve, J., & Fetterer, F. (2007). Whither Arctic sea ice? A clear signal of decline regionally, seasonally and extending beyond the satellite record. *Annals of Glaciology*, *46*, 428–434. https://doi.org/10.3189/172756407782871170
Menemenlis, D., Campin, J. M., Heimbach, P., Hill, C., Lee, T., Nguyen, A., . . . Zhang, H. (2008). ECCO2: High resolution global ocean and sea ice data synthesis. *Mercator Ocean Quarterly Newsletter*, *31*, 13–21.
Moon, W., & Wettlaufer, J. S. (2011). A low-order theory of Arctic sea ice stability. *Europhysics Letters*, *96*(3), 39001.
Moon, W., & Wettlaufer, J. S. (2014). On the nature of the sea ice albedo feedback in simple models. *Journal of Geophysical Research: Oceans*, *119*, 5555–5562. https://doi.org/10.1002/2014JC009964
Moon, W., & Wettlaufer, J. S. (2017). A unified nonlinear stochastic time series analysis for climate science. *Scientific Reports*, *7*, 44228, https://doi.org/10.1038/srep44228
Niebauer, H. J. (1982). Wind and melt driven circulation in a marginal sea ice edge frontal system: A numerical model. *Continental Shelf Research*, *1*(1), 49–98.
Niebauer, H. J., & Smith, W. O. (1989). A numerical model of mesoscale physical biological interactions in the Fram Strait marginal ice zone. *Journal of Geophysical Research*, *94*(C11), 16151–16175.
Nurser, A. J. G., & Bacon, S. (2014). The Rossby radius in the Arctic Ocean. *Ocean Science*, *10*(6), 967–975.
Overland, J. E., & Wang, M. (2013). When will the summer Arctic be nearly sea ice free? *Geophysical Research Letters*, *40*, 2097–2101. https://doi.org/10.1002/grl.50316
Park, H. S., & Stewart, A. L. (2016). An analytical model for wind-driven Arctic summer sea ice drift. *Cryosphere*, *10*(1), 227–244.
Perovich, D., RichterMenge, J., Polashenski, C., Elder, B., Arbetter, T., & Brennick, O. (2014). Sea ice mass balance observations from the North Pole Environmental Observatory. *Geophysical Research Letters*, *41*, 2019–2025. https://doi.org/0.1002/2014GL059356
Perovich, D. K., Light, B., Eicken, H., Jones, K. F., Runciman, K., & Nghiem, S. V. (2007). Increasing solar heating of the Arctic Ocean and adjacent seas, 19792005: Attribution and role in the ice albedo feedback. *Geophysical Research Letters*, *34*, L19505. https://doi.org/10.1029/2007GL031480
Polyakov, I. V. Pnyushkov, A. V., Alkire, M. B., Ashik, I. M., Baumann, T. M., Carmack, E. C., . . . Yulin, A. (2017). Greater role for Atlantic inflows on sea-ice loss in the Eurasian Basin of the Arctic Ocean. *Science*, *356*(6335), 285–291.
Serreze, M. C., & Barry, R. G. (2011). Processes and impacts of Arctic amplification: A research synthesis. *Global and Planetary Change*, *77*, 85–96. https://doi.org/10.1016/j.gloplacha.2011.03.004
Serreze, M. C., & Stroeve, J. (2015). Arctic sea ice trends, variability and implications for seasonal ice forecasting. *Philosophical Transactions of the Royal Society A*, *373*(2045), 20140159.
Shimada, K., Kamoshida, T., Itoh, M., Nishino, S., Carmack, E., McLaughlin, F. A., . . . Proshutinsky, A. (2006). Pacific Ocean inflow: Influence on catastrophic reduction of sea ice cover in the Arctic Ocean. *Geophysical Research Letters*, *33*, L08605. https://doi.org/10.1029/2005GL025624
Smith, D. C. IV., & Bird, A. A. (1991). The interaction of an ocean eddy with an ice edge ocean jet in a marginal ice zone. *Journal of Geophysical Research*, *96*(C3), 4675–4689. https://doi.org/10.1029/90JC02262
Spreen, G., Kwok, R., & Menemenlis, D. (2011). Trends in Arctic sea ice drift and role of wind forcing: 19922009. *Geophysical Research Letters*, *38*, L19501. https://doi.org/10.1029/2011GL048970
Steele, M., & Ermold, W. (2015). Loitering of the retreating sea ice edge in the Arctic Seas. *Journal of Geophysical Research: Oceans*, *120*, 7699–7721. https://doi.org/10.1002/2015JC011182
Stroeve, J., Hamilton, L. C., Bitz, C. M., & BlanchardWrigglesworth, E. (2014). Predicting September sea ice: Ensemble skill of the SEARCH sea ice outlook 20082013. *Geophysical Research Letters*, *41*, 2411–2418. https://doi.org/10.1002/2014GL059388
Stroeve, J. C., Kattsov, V., Barrett, A., Serreze, M., Pavlova, T., Holland, M., & Meier, W. N. (2012). Trends in Arctic sea ice extent from CMIP5, CMIP3 and observations. *Geophysical Research Letters*, *39*, L16502. https://doi.org/10.1029/2012GL052676
Stroeve, J. C., Markus, T., Boisvert, L., Miller, J., & Barrett, A. (2014). Changes in Arctic melt season and implications for sea ice loss. *Geophysical Research Letters*, *41*, 1216–1225. https://doi.org/10.1002/2013GL058951
Stroeve, J. C., Serreze, M. C., Holland, M. M., Kay, J. E., Malanik, J., & Barrett, A. P. (2012). The Arctics rapidly shrinking sea ice cover: A research synthesis. *Climatic Change*, *110*(3), 1005–1027.
Strong, C., & Rigor, I. G. (2013). Arctic marginal ice zone trending wider in summer and narrower in winter. *Geophysical Research Letters*, *40*, 4864–4868. https://doi.org/10.1002/grl.50928
Taylor, G. I. (1922). Diffusion by continuous movements. *Proceedings of the London Mathematical Society*, *2*(1), 196–212.
Taylor, J. R., & Ferrari, R. (2010). Buoyancy and wind-driven convection at mixed layer density fronts. *Journal of Physical Oceanography*, *40*(6), 1222–1242.
Taylor, J. R., & Sarkar, S. (2008). Stratification effects in a bottom Ekman layer. *Journal of Physical Oceanography*, *38*(11), 2535–2555.
Taylor, K. E., Stouffer, R. J., & Meehl, G. A. (2012). An overview of CMIP5 and the experiment design. *Bulletin of the American Meteorological Society*, *93*, 485–498. https://doi.org/10.1175/BAMS-D-11-00094.1
Thomas, D. N. (Ed.) (2016). *Sea ice. Chapter 5: The sea ice-ocean boundary layer*. Hoboken, NJ: John Wiley.
Thomas, L. N., Tandon, A., & Mahadevan, A. (2008). Submesoscale processes and dynamics. In M. W. Hecht & H. Hasumi (Eds.) *Ocean modeling in an eddying regime, Geophysical Monograph Series* (Vol. 177, pp. 17–38). Washington, DC: American Geophysical Union. https://doi.org/10.1029/177GM04
Thompson, A. F., Lazar, A., Buckingham, C. E., Naveira Garabato, A. C., Damerell, G. M., & Heywood, K. J. (2016). Open-ocean submesoscale motions: A full seasonal cycle of mixed layer instabilities from gliders. *Journal of Physical Oceanography*, *46*, 1285–1307.

Thorndike, A. S., & Colony, R. (1982). Sea ice motion in response to geostrophic winds. *Journal of Geophysical Research*, *87*(C8), 5845–5852.
Tietsche, S., Day, J. J., Guemas, V., Hurlin, W. J., Keeley, S. P. E., Matei, D., . . . Hawkins, E. (2014). Seasonal to interannual Arctic sea ice predictability in current global climate models. *Geophysical Research Letters*, *41*, 1035–1043. https://doi.org/10.1002/2013GL058755
Toole, J. M., Krishfield, R. A., Timmermans, M. L., & Proshutinsky, A. (2011). The ice-tethered profiler: Argo of the Arctic. *Oceanography*, *24*(3), 126–135.
Towns, J., Cockerill, T., Dahan, M., Foster, I., Gaither, K., Grimshaw, A., . . . Wilkins-Diehr, N. (2014). XSEDE: Accelerating scientific discovery. *Computing in Science & Engineering*, *16*(5), 62–74.
Toyota, T., Haas, C., & Tamura, T. (2011). Size distribution and shape properties of relatively small sea-ice floes in the Antarctic marginal ice zone in late winter. *Deep Sea Research Part II: Topical Studies in Oceanography*, *58*(9), 1182–1193.
Toyota, T., Takatsuji, S., & Nakayama, M. (2006). Characteristics of sea ice floe size distribution in the seasonal ice zone. *Geophysical Research Letters*, *33*, L02616. https://doi.org/10.1029/2005GL024556
Tsamados, M., Feltham, D. L., Schroeder, D., Flocco, D., Farrell, S. L., Kurtz, N., . . .Bacon, S. (2014). Impact of variable atmospheric and oceanic form drag on simulations of Arctic sea ice. *Journal of Physical Oceanography*, *44*(5), 1329–1353.
Turner, J., Bracegirdle, T. J., Phillips, T., Marshall, G. J., & Hosking, J. S. (2013). An initial assessment of Antarctic sea ice extent in the CMIP5 models. *Journal of Climate*, *26*(5), 1473–1484.
Vallis, G. K. (Ed.) (2006). *Atmospheric and oceanic fluid dynamics* (pp. 770). Cambridge, UK: Cambridge University Press.
Zhang, J., Ashjian, C., Campbell, R., Spitz, Y. H., Steele, M., & Hill, V. (2015). The influence of sea ice and snow cover and nutrient availability on the formation of massive under-ice phytoplankton blooms in the Chukchi Sea. *Deep Sea Research Part II: Topical Studies in Oceanography*, *118*, 122–135.
Zhang, J., & Hibler, W. D. III, (1997). On an efficient numerical method for modeling sea ice dynamics. *Journal of Geophysical Research*, *102*(C4), 8691–8702.